

# CONSTRAINING THE ACCRETION FLOW IN SGR A\* BY GENERAL RELATIVISTIC DYNAMICAL AND POLARIZED RADIATIVE MODELING

ROMAN V. SHCHERBAKOV<sup>1</sup>, ROBERT F. PENNA<sup>1</sup>, JONATHAN C. MCKINNEY<sup>2</sup>

*Draft version March 18, 2019*

## ABSTRACT

The constraints on the Sgr A\* black hole (BH) and accretion flow parameters are found by fitting polarized sub-mm observations. First, we compile a mean Sgr A\* spectrum by averaging observations over many epochs from reports in 29 papers, which results in a robust spectrum determination with small standard errors. We find the mean flux  $F_\nu$ , linear polarization (LP) fractions, circular polarization (CP) fractions, and electric vector position angles (EVPA). We run three-dimensional general relativistic magnetohydrodynamical (3D GRMHD) simulations for dimensionless spins  $a_* = 0, 0.5, 0.7, 0.9, 0.98$  over a  $20000M$  time interval, construct averaged dynamical models, perform radiative transfer, and explore the parameter space of spin  $a_*$ , inclination angle  $\theta$ , position angle (PA), accretion rate  $\dot{M}$ , and electron temperature  $T_e$  at radius  $6M$ . A new general relativistic polarized radiative transfer code is implemented to simulate polarized fluxes from the averaged models. Averaged dynamical models are compiled by averaging simulations over time. In the main “RMS-field” model, the magnetic field is directed along the time-averaged field and has a strength of the root-mean-square field. A model with linear time-averaged magnetic field is also tested. We perform  $\chi^2$  per degrees of freedom (dof) statistical analysis to quantify the goodness of models in fitting mean fluxes, LP and CP fractions between 88 GHz to 857 GHz. The RMS-field model favors spin  $a_* = 0.9$  with minimum  $\chi^2/\text{dof} \approx 4.0$ . Correspondent 90% confidence intervals for spin  $a_* = 0.9$  simulation are  $\theta = 53^\circ \pm 3^\circ$ ,  $\text{PA} = 121^\circ \pm 20^\circ$ ,  $\dot{M} = (1.09 \pm 0.13) \times 10^{-8} M_\odot \text{year}^{-1}$ ,  $T_e = (4.62 \pm 0.56) \cdot 10^{10}$  K at  $6M$ . The linear averaged magnetic field model with same spin gives similar expectation values. By combining the results from spin  $a_* = 0.9$  models we obtain the conservative estimates:  $\theta = 50^\circ - 59^\circ$ ,  $\text{PA} = 101^\circ - 143^\circ$ ,  $\dot{M} = (0.9 - 1.7) \times 10^{-8} M_\odot \text{year}^{-1}$ ,  $T_e = (2.7 - 5.2) \cdot 10^{10}$  K at  $6M$ . Fitting only the flux spectrum without LP and CP fractions results in the best  $\chi^2_F/\text{dof} < 1$  for  $a_* = 0.7, 0.9, 0.98$  and much wider confidence intervals, thus polarization is an essential component for constraining the spin, disk orientation, and flow properties. We identify physical phenomena leading to matched LP fraction, CP fraction, EVPA by sequentially switching off radiative transfer effects. In particular, the observed amount of CP is produced by Faraday conversion. The emission region size at 230 GHz of the best-fitting RMS-field model with spin  $a_* = 0.9$  is consistent with the size  $37\mu\text{as}$  observed by VLBI methods.

*Subject headings:* accretion, accretion disks – black hole physics – Galaxy: center – radiative transfer – relativistic processes — polarization

## 1. INTRODUCTION

Our Galactic Center black hole is one of many inactive galactic cores, the only distinctive feature being its proximity to us. The mass of the black hole (BH) is known to be  $M \approx 4.5 \cdot 10^6 M_\odot$  (Ghez et al. 2008) and the spin is uncertain. It resides at a distance of about  $d \approx 8.4$  kpc. Because of such proximity, many observations of the source were made in all wavelengths, which are not completely obscured by absorption:  $\gamma$ -rays, X-rays, IR, (sub-)mm, and radio. The origins of X-rays are bremsstrahlung from hot gas near the radius of BH gravitational influence (Narayan, Yi & Mahadevan 1995; Narayan et al. 1998; Shcherbakov & Baganoff 2010) and Compton-scattered

emission close to the horizon (Moscibrodzka et al. 2009). X-rays at large radius are spatially resolved, which gives an opportunity to test dynamical models far from the black hole (Shcherbakov & Baganoff 2010). The sub-mm emission is cyclo-synchrotron originating close to the black hole. Cyclo-synchrotron emission is polarized, both linear and circular polarizations were observed from Sgr A\* at several sub-mm wavelengths. The accretion flow was recently resolved at 230 GHz (Doeleman et al. 2008). General relativistic (GR) effects were deemed necessary to explain the small size with full width at half maximum (FWHM) of  $37\mu\text{as}$ . The radio emission is also produced by cyclo-synchrotron, but at larger distance from the BH. Thus, to study the effects of GR, one should model sub-mm polarized observations while also considering the amount of Compton-scattered X-rays. Modeling the sub-mm in the range 88 GHz to 857 GHz is the goal of the present paper.

First, we need to understand which observations to fit. Sgr A\* is a variable source with a variability amplitude routinely reaching 30% in sub-mm. A popular approach is to fit simultaneous observations (e.g.

rshcherbakov@cfa.harvard.edu

<sup>1</sup> <http://www.cfa.harvard.edu/%7Ershcherb/rpenna@cfa.harvard.edu>

Harvard-Smithsonian Center for Astrophysics, 60 Garden Street, Cambridge, MA 02138, USA

<sup>2</sup> jmckinne@stanford.edu

Department of Physics and Kavli Institute for Particle Astrophysics and Cosmology, Stanford University, Stanford, CA 94305-4060, USA; Chandra Fellow

Yuan, Quataert & Narayan 2004; Broderick et al. 2009), in particular the set from Falcke et al. (1998). However, one cannot easily combine two sets of observations in such an approach: the addition of a new frequency would require redoing observations of every other frequency at that instant of time. Simultaneous observations of linear polarization (LP) and circular polarization (CP) at several frequencies were not yet performed. Thus, it is quite reasonable to consider non-simultaneous statistics of all observations at all frequencies instead and find the mean values and standard errors of quantities at each frequency. We check that samples of observed fluxes and LP fractions are consistent with a Gaussian distribution at  $\nu \geq 88$  GHz.

A good GR dynamical model of accretion is required to reproduce the observations. There are now numerous accretion flow models applicable to the Galactic Center: advection-dominated accretion flow (ADAF) (Narayan & Yi 1995), adiabatic inflow-outflow solution (ADIOS) (Blandford & Begelman 1999), jet-ADAF (Yuan, Markoff & Falcke 2002), jet (Maitra, Markoff & Falcke 2009), and the models directly based on numerical simulations. These quasi-analytical models in general have a large number of free parameters and also incorporate many assumptions that are not generally justifiable (Huang et al. 2008, 2009a), which leads to unreliable constraints on the properties of the black hole accretion flow. The numerical simulations require fewer inputs and settle into a quasi-steady accretion, which justifies their use. GRMHD simulations, like those performed in McKinney & Blandford (2009); Fragile et al. (2009); Noble & Krolik (2009); Moscibrodzka et al. (2009); Penna et al. (2010), are necessary for modeling matter infall onto a rotating BH. The behavior of accretion is also different between two-dimensional and three-dimensional models (Igumenshchev 2008) due to Cowling’s anti-dynamo theorem, so we model the flow in three dimensions. Numerical simulations are limited to a region relatively close to the BH (Dexter et al. 2009; Moscibrodzka et al. 2009), whereas some emission and some Faraday rotation might happen far from the BH. Thus, we analytically extend the modeled region out to  $20000M$ , do radiative transfer, and find the best fit to the data. The extension to large radius allows us to define the electron temperature more consistently (Sharma et al. 2007). We find a posteriori (see Appendix A) that the simulated polarized spectra are insensitive to variations of analytic extensions of density and temperature, but may depend on the extension of the magnetic field.

A good dynamical model does not eliminate the uncertainty of comparing to data. Indeed, correct radiative transfer and statistical analysis are necessary for such a comparison. The simplest Newtonian radiation consideration (Yuan, Quataert & Narayan 2004) does not provide a means to treat radiation close to the BH. A quasi-Newtonian approach offers some improvement (Goldston, Quataert & Igumenshchev 2005; Chan et al. 2009). General relativistic treatments of unpolarized light (Fuerst & Wu 2004; Dexter et al. 2009; Dolence et al. 2009) capture most GR effects, but only polarized general relativistic radiative transfer (Broderick et al. 2009; Gammie & Leung 2010; Shcherbakov & Huang 2011) is exact and captures

all GR phenomena. The present paper adopts this approach. We are able to compare the results of modeling to extensive polarization data, constraining much better the flow parameters and spin. In fact, fitting only the total flux spectrum might not constrain the spin. Spin values from  $a_* = 0$  (Broderick et al. 2009) to  $a_* = 0.9$  (Moscibrodzka et al. 2009) are found in the literature. Other radiation ingredients may include Comptonization (Moscibrodzka et al. 2009) and radiation from non-thermal electrons (Mahadevan 1998; Özel, Psaltis & Narayan 2000; Yuan, Quataert & Narayan 2004). We do not consider non-thermal electrons, but find that strong radio emission at  $\nu < 50$  GHz is produced in polar flow regions even by thermal electrons. Emissivities are calculated in synchrotron approximation (Legg & Westfold 1968; Sazonov 1969; Pacholczyk 1970; Melrose 1971) with an exact thermal electron distribution. Emissivities in the synchrotron approximation are very close to the exact cyclo-synchrotron emissivities (Leung, Gammie & Noble 2009; Shcherbakov & Huang 2011), so we use the former. However, the exact Faraday rotation and conversion expressions are employed (Shcherbakov 2008), as no similar approximations exist for them.

The comparison of simulations to observations were done in the past “by eye” in studies of Sgr A\* until quite recently, when Broderick et al. (2009) followed by Dexter et al. (2009) introduced statistical analyses. We extend their approach by incorporating the statistics of LP and CP fractions and comparing simulated spectra to observed ones at many frequencies simultaneously. After checking for normality of observations, computing their means and standard errors, we employ  $\chi^2$  statistics. We search the space of all parameters: spin  $a_*$ , inclination  $\theta$ , ratio of proton to electron temperatures  $T_p/T_e$  at distance  $6M$  from the center, and accretion rate  $\dot{M}$  to find the minimum  $\chi^2$  models. We find models with  $\chi^2$  relatively close to unity. Then we integrate the  $\chi^2$  probability density function (PDF) over the entire parameter space and compute the expectation values of model parameters together with the uncertainties and 90% confidence intervals. Full statistical analysis is performed in the present work.

The paper is constructed as follows. We summarize the observational manifestations of the accretion flow in the sub-mm in § 2. The 3D GRMHD simulations are described in § 3 together with the physically-motivated extension to large radii, the electron heating prescription, and the flow averaging prescription. We run simulations for dimensionless spins  $a_* = a/M = 0, 0.5, 0.7, 0.9, 0.98$ . As the required CPU time to compute the average of simulated spectra via many snapshots to mimic observations is prohibitively large, we perform radiative transfer over averaged models. The GR polarized radiative transfer technique is elaborated upon in § 5. The statistical analysis is presented in § 6. The set of observations considered consists of the spectral energy distribution (SED) within the 88 GHz to 857 GHz frequency range, linear polarization (LP) fractions at 88 GHz, 230 GHz, and 349 GHz, and circular polarization (CP) fractions at 230 GHz and 349 GHz. In § 7 we discuss numerous results: the best fits to observations, the behaviors of  $\chi^2$  near the best fits, the importance of various physical ef-

fects in producing the observed CP, LP, and electric vector position angle (EVPA), expectation values of quantities and confidence intervals, and image size estimates. We show the actual images of total and polarized intensities and generate movies. Discussion in § 8 compares the results to previous estimates, emphasizes the significance of polarization, notes the sources of errors, and outlines prospects for future work. We note that fitting only the total flux provides very loose constraints on the flow. In Appendix A we perform a number of convergence tests for radial extension of the dynamical model and GR polarized radiative transfer code. Throughout the paper we measure distance and time in the units of BH mass  $M$  by setting the speed of light and gravitational constant to unity.

## 2. OBSERVATIONS

Sgr A\* is known to be a highly variable source, yet quiescent models of Sgr A\* emission are popular and useful. Unlike the drastic variations of X-ray and NIR fluxes (Baganoff et al. 2001; Genzel et al. 2003), sub-mm fluxes do not vary by more than a factor of 2 – 3 (Zhao et al. 2003). Thus, it is reasonable to approximate the distribution of observed fluxes at each frequency and polarization type by a Gaussian, find the mean and the standard error and use the framework of standard  $\chi^2$  analysis. Previously, the flux spectra were modeled by Yuan, Quataert & Narayan (2004); Broderick et al. (2009). However, both papers summarize a limited set of observations and do not perform any averaging. Sub-mm flux data reported in Yuan, Quataert & Narayan (2004) consists of a short set of observations by Falcke et al. (1998) and one set of SMA observations by Zhao et al. (2003). Broderick et al. (2009) adds to these the rest of SMA total flux data (Marrone et al. 2006a,b, 2007, 2008). Thus, only 6 out of at least 29 papers on sub-mm observations of Sgr A\* were employed. Our work computes a properly averaged spectrum based on all papers to date reporting sub-mm observations of Sgr A\*.

The reported observations vary greatly in the covered period from several hours (An et al. 2005) to several years (Zhao et al. 2003; Krichbaum et al. 2006). We know that variations of a factor of 2 may happen within several hours (Yusef-Zadeh et al. 2009), whereas more than a factor of several are never observed in the sub-mm. Thus, fluxes observed more than a day apart are weakly correlated. A question of autocorrelation timescales will be addressed in more detail in future work. We, therefore, consider the following averaging technique to robustly sample the distributions of fluxes. First, we define groups of close frequencies, where frequencies are different by no more than several percent from the mean. There are 11 groups (see Table 1). We have excluded papers reporting frequencies far from the mean of each group. In particular, 94 GHz and 95 GHz observations in Li et al. (2008); Falcke et al. (1998) and the 112 GHz observations in Bower et al. (2001) are excluded. A mean frequency is ascribed to represent each group. Then we take all the reported observations of each polarization type (total flux, LP and CP fraction, EVPA) for each group and draw the largest sample of fluxes/polarization fractions observed more than one day apart. When several fluxes are reported over a period of several hours (Yusef-Zadeh et al. 2009), we normally only draw one

data point from the very beginning of such an observation. There are some unreliable observations over the set of papers. Often unreliable data is produced by observing in sub-mm with large beam size. Light from Sgr A\* is blended with dust and other sources. For example, SMT data (Yusef-Zadeh et al. 2009), early CSO measurements (Serabyn et al. 1997), and early JCMT measurements (Aitken et al. 2000) may have such issues. We exclude these data from the sample. The interferometric observations, especially with VLBI, help to reduce an error of otherwise unreliable observations, e.g. with BIMA array (Bower et al. 2001). However, some inconsistencies still exist for simultaneous observations at the same frequency with different instruments (Yusef-Zadeh et al. 2009).

After a robust sample of fluxes, polarization fractions, and EVPA angles is found for each frequency group, we compute the mean, the standard error and check (by Kolmogorov-Smirnov test) that the data are consistent with the resultant Gaussian distribution. For LP fractions we consider the statistics of  $\log(\text{LP})$ . The summary of results is presented in Table 1. CP fractions of  $-1.2\%$  at 230 GHz and  $-1.5\%$  at 349 GHz are based on preliminary work by SMA collaboration with the reported error  $\pm 0.3\%$  of instrumental nature. The p-values of the Kolmogorov-Smirnov consistency test are above 0.05 for  $\log(\text{LP})$  and EVPA in each frequency group, which shows the consistency of sample fluxes/LP fractions with Gaussians and validates the  $\chi^2$  analysis. Also,  $p > 0.05$  holds for fluxes at all frequencies except  $\nu = 14.90$  GHz,  $\nu = 22.50$  GHz,  $\nu = 43$  GHz. Exceptionally large samples of  $> 100$  fluxes are reported in Herrnstein et al. (2004) for those frequencies. The flux distribution at  $\nu \leq 43$  GHz is found to be bimodal and inconsistent with a Gaussian. However,  $p = 0.7$  for the Kolmogorov-Smirnov test at  $\nu = 230$  GHz despite a large sample of 50 fluxes. Thus, we prove that the current state of observations supports Gaussian distributions of  $F_\nu$ ,  $\log(\text{LP})$ , CP, and EVPA for frequencies  $\nu \geq 88$  GHz and allows for  $\chi^2$  statistical analysis based on computed means and standard errors. Note also, that standard errors in our flux samples are smaller than the error bars of old observations (Falcke et al. 1998; Yuan, Quataert & Narayan 2004; Broderick et al. 2009), but the errors are still larger compared to contemporary single-observation instrumental errors (Marrone et al. 2007). Thus, we do not incorporate instrumental error in our estimates of an error of a flux sample mean. The same is true for  $\log(\text{LP})$  and EVPA. We do not incorporate the source size measurements (Doeleman et al. 2008) in calculating the  $\chi^2$ , but check that the best fit model is consistent with those observations. Figure 1 shows a compilation of the mean quantities with their Gaussian standard errors. The data are represented by both error bars and the interpolated shaded area in between. A red dashed curve on  $F_\nu$  plot represents the analytic approximation  $F_\nu = 0.248\nu^{0.45} \exp(-(\nu/1100)^2)$ , where flux is in Jy and frequency is in GHz.

## 3. DYNAMICAL MODEL: 3D GRMHD SIMULATIONS

Our radiative transfer calculations take the results of simulations of accretion flows onto black holes as input. These simulations are similar to those in Penna et al. (2010). We review the methodology.

**Table 1**  
Summary of Sgr A\* radio/sub-mm observations

$\nu$ [GHz]	Telescopes	$F_\nu$ [Jy]	LP [%]	CP [%]	EVPA [°]
8.45	VLA	$0.683 \pm 0.032$ (Serabyn et al. 1997; Falcke et al. 1998; Bower et al. 1999a; An et al. 2005)	...	$-0.26 \pm 0.06^b$ (Bower et al. 1999a)	...
14.90	VLBA, VLA	$0.871 \pm 0.012^a$ (Serabyn et al. 1997; Falcke et al. 1998; Bower et al. 2002; Herrnstein et al. 2004; An et al. 2005; Yusef-Zadeh et al. 2009)	...	$-0.62 \pm 0.26^b$ (Bower et al. 2002)	...
22.50	VLBA, VLA	$0.979 \pm 0.016^a$ (Serabyn et al. 1997; Falcke et al. 1998; Bower et al. 1999b; Herrnstein et al. 2004; An et al. 2005; Lu et al. 2008; Yusef-Zadeh et al. 2007, 2009)	$0.20 \pm 0.01^b$ (Bower et al. 1999b; Yusef-Zadeh et al. 2007)	...	...
43	GMVA, VLBA, VLA	$1.135 \pm 0.026^a$ (Falcke et al. 1998; Lo et al. 1998; Bower et al. 1999b; Herrnstein et al. 2004; An et al. 2005; Shen et al. 2005; Krichbaum et al. 2006; Yusef-Zadeh et al. 2007; Lu et al. 2008; Yusef-Zadeh et al. 2009)	$0.50^{+0.27^b}_{-0.17}$ (Bower et al. 1999b; Yusef-Zadeh et al. 2007)	...	...
88	BIMA, MPIfR, VLBA, VLA, Nobeyama, NMA, CARMA	$1.841 \pm 0.080$ (Falcke et al. 1998; Krichbaum et al. 1998; Bower et al. 1999b; Doeleman et al. 2001; Miyazaki et al. 2004; Shen et al. 2005; Krichbaum et al. 2006; Macquart et al. 2006; Lu et al. 2008; Yusef-Zadeh et al. 2009)	$1.03^{+0.21^c}_{-0.18}$ (Bower et al. 1999b; Macquart et al. 2006)	...	$-4^d$ (Bower et al. 1999b; Shen et al. 2005; Macquart et al. 2006)
102	OVRO, CSO-JCMT, Nobeyama, NMA, IRAM	$1.91 \pm 0.15$ (Serabyn et al. 1997; Falcke et al. 1998; Miyazaki et al. 2004; Mauerhan et al. 2005; Yusef-Zadeh et al. 2009)	...	...	...
145	Nobeyama, NMA, IRAM, JCMT	$2.28 \pm 0.26$ (Falcke et al. 1998; Aitken et al. 2000; Miyazaki et al. 2004; Yusef-Zadeh et al. 2009)	...	...	...
230	IRAM, JCMT, BIMA, SMA, OVRO	$2.64 \pm 0.14$ (Serabyn et al. 1997; Falcke et al. 1998; Aitken et al. 2000; Bower et al. 2003, 2005; Zhao et al. 2003; Krichbaum et al. 2006; Marrone et al. 2006a, 2007, 2008; Doeleman et al. 2008; Yusef-Zadeh et al. 2009)	$7.02^{+0.63^c}_{-0.58}$ (Bower et al. 2003, 2005; Marrone et al. 2007, 2008)	$-1.2 \pm 0.3^p$ (Munoz et al. 2009), Munoz et al. 2010, in prep.)	$111.5 \pm 5.3$ (Bower et al. 2003, 2005; Marrone et al. 2007, 2008)
349	SMA, CSO, JCMT	$3.18 \pm 0.12$ (Aitken et al. 2000; An et al. 2005; Marrone et al. 2006b, 2007, 2008; Yusef-Zadeh et al. 2009)	$6.14^{+0.75^c}_{-0.67}$ (Marrone et al. 2006b, 2007)	$-1.5 \pm 0.3^b$ (Munoz et al. 2010, in prep.)	$146.9 \pm 2.2$ (Marrone et al. 2006b, 2007)
674	CSO, SMA	$3.29 \pm 0.35$ (Marrone et al. 2006a, 2008; Yusef-Zadeh et al. 2009)	...	...	...
857	CSO	$2.87 \pm 0.24$ (Serabyn et al. 1997; Marrone et al. 2008; Yusef-Zadeh et al. 2009)	...	...	...

<sup>a</sup>Flux observations at 14.9, 22.5, 43 GHz are inconsistent with a Gaussian distribution (Herrnstein et al. 2004), while other fluxes, CP fractions and logarithms of LP fractions are consistent with Gaussian distributions.

<sup>b</sup>The uncertainty of the mean in these quantities is given by instrumental errors.

<sup>c</sup>Standard errors are computed for logarithms of LP fractions.

<sup>d</sup>The mean EVPA at 88 GHz is uncertain due to the  $\pm 180^\circ$  degeneracy; e.g. the reported EVPA =  $80^\circ$  could as well be interpreted as  $-100^\circ$ .

### 3.1. Governing equations

We simulate radiatively inefficient accretion flows (RIAFs) onto rotating black holes using a three-dimensional fully general relativistic code (see §3.3). The black hole is described by the Kerr metric. We work with Heaviside-Lorentz units. Our five simulations correspond to different choices of the dimensionless black hole spin parameter:  $a_* = 0, 0.5, 0.7, 0.9,$  and  $0.98$ . The self-gravity of the RIAF is ignored.

The RIAF is a magnetized fluid, so we solve the GRMHD equations of motion (Gammie et al. 2003). Mass conservation gives:

$$\nabla_\mu(\rho u^\mu) = 0, \quad (1)$$

where  $\rho$  is the fluid frame rest-mass density,  $u^\mu$  is the contravariant 4-velocity, and  $\nabla_\mu$  is the covariant deriva-

tive. Energy-momentum conservation gives

$$\nabla_\mu T_\nu^\mu = 0, \quad (2)$$

where the stress energy tensor  $T_\nu^\mu$  includes both matter and electromagnetic terms,

$$T_\nu^\mu = (\rho + u_g + p_g + b^2)u^\mu u_\nu + (p_g + b^2/2)\delta_\nu^\mu - b^\mu b_\nu, \quad (3)$$

where  $u_g$  is the internal energy density and  $p_g = (\Gamma - 1)u_g$  is the ideal gas pressure with  $\Gamma = 4/3$ <sup>3</sup>. The contravariant fluid-frame magnetic 4-field is given by  $b^\mu$  and is related to the lab-frame 3-field via  $b^\mu = B^\nu h_\nu^\mu / u^t$  where  $h_\nu^\mu = u^\mu u_\nu + \delta_\nu^\mu$  is a projection tensor, and  $\delta_\nu^\mu$  is the Kronecker delta function (Gammie et al. 2003). We often employ  $\mathbf{b}$  below, which is the orthonormal magnetic field vector in a comoving locally flat reference

<sup>3</sup> Models with  $\Gamma = 5/3$  show some minor differences compared to models with  $\Gamma = 4/3$  (McKinney & Gammie 2004; Mignone & McKinney 2007).

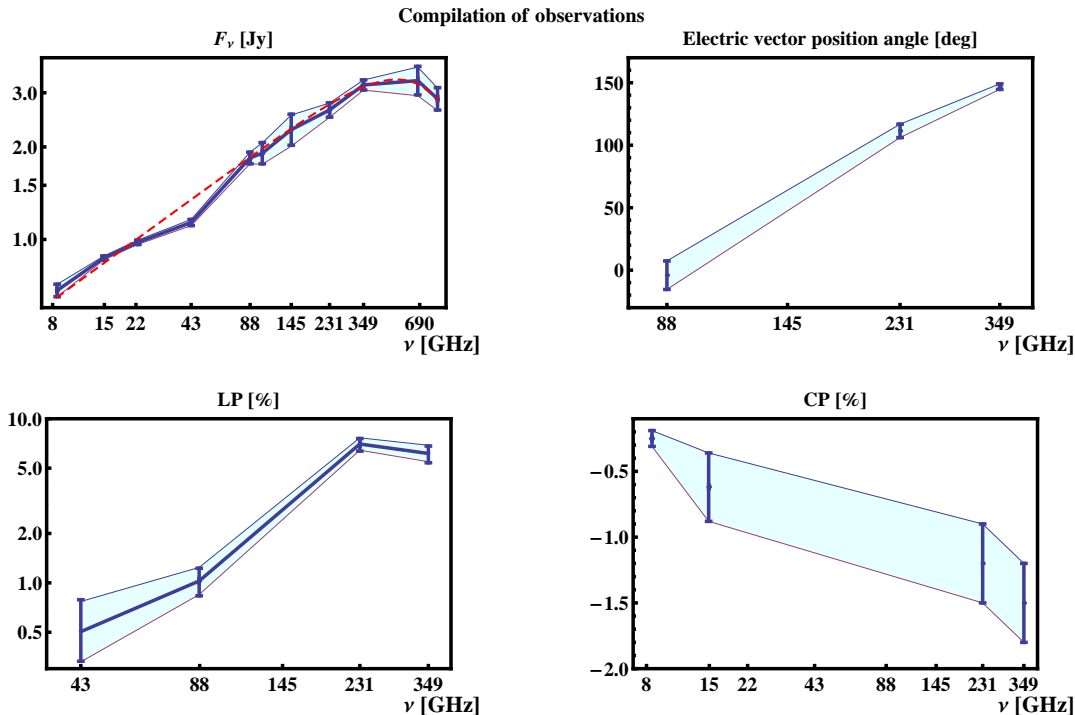


**Figure 1.** Mean observed SEDs of specific flux  $F_\nu$ , linear polarization (LP) fraction, electric vector position angle (EVPA), and circular polarization (CP) fraction. The error bars show the  $1\sigma$  standard error of the mean. The dashed line on the  $F_\nu$  plot represents the analytic approximation  $F_\nu(\text{Jy}) = 0.248\nu^{0.45} \exp(-(\nu/1100)^2)$  for frequency  $\nu$  in GHz (not the simulated SED). As noted in Table 1, the error is instrumental for CP, whereas it is computed from a sample of observed quantities for flux, LP and EVPA.

frame (Penna et al. 2010). The magnetic energy density ( $u_b$ ) and magnetic pressure ( $p_b$ ) are then given by  $u_b = p_b = b^2 b_\mu/2 = b^2/2 = \mathbf{b}^2/2$ . Note that the angular velocity of the gas is  $\Omega = u^\phi/u^t$ .

Magnetic flux conservation is given by the induction equation

$$\partial_t(\sqrt{-g}B^i) = -\partial_j[\sqrt{-g}(B^i v^j - B^j v^i)], \quad (4)$$

where  $v^i = u^i/u^t$ , and  $g = \text{Det}(g_{\mu\nu})$  is the determinant of the metric. No explicit resistivity or viscosity is included.

In Penna et al. (2010), we studied both RIAFs and geometrically thin, radiatively efficient disks. For the later case, a cooling term was added to the energy-momentum equation (2) to describe radiative losses and keep the disk thin. The current set of models are all RIAFs, so no cooling term is needed, energy generated by viscous dissipation is advected along with the flow or transported out due to convection or in a wind.

### 3.2. Physical models

The initial mass distribution is an isentropic equilibrium torus (Chakrabarti 1985a,b; De Villiers, Hawley & Krolik 2003) with pressure  $p = K_0 \rho^{4/3}$  for  $K_0 = 0.009$ . The torus inner edge is at  $r_{\text{in}} = 20M$  and maximum density and pressure are at  $R_{\text{max}} = 65M$ . We initialize the solution so that  $\rho = 1$  at the pressure maximum. As in Chakrabarti (1985a), the angular velocity distribution of the initial torus is a power law, where for the Chakrabarti (1985a)  $q$ -parameter we choose  $q = 1.65$  (At large radii  $\Omega \sim (r/M)^{-q}$ ). The thickness of the torus at the

pressure maximum is then  $|h/r| = 0.3$ , where

$$|h/r| \equiv \frac{\int \int \int |\theta - \pi/2| \rho(r, \theta, \phi) dA_{\theta\phi} dt}{\int \int \int \rho(r, \theta, \phi) dA_{\theta\phi} dt}, \quad (5)$$

where  $dA_{\theta\phi} \equiv \sqrt{-g} d\theta d\phi$  is an area element in the  $\theta - \phi$  plane, and the integral over  $dt$  is a time average over the period when the disk is in a steady state (see §3.6). A tenuous atmosphere fills the space outside the torus. It has the same polytropic equation of state as the torus,  $p = K_0 \rho^\Gamma$ , with  $\Gamma = 4/3$ , and an initial rest-mass density of  $\rho = 10^{-6}(r/M)^{-3/2}$ , corresponding to a Bondi-like atmosphere. The torus is threaded with three loops of weak, poloidal magnetic field: the initial gas-to-magnetic pressure ratio is  $\beta = p_{g,\text{max}}/p_{b,\text{max}} = 100$ , where  $p_{\text{max}}$  and  $p_{b,\text{max}}$  are the maximum values of the gas and magnetic pressure in the torus. This approach to normalizing the initial field is used in many other studies (Gammie et al. 2003; McKinney & Gammie 2004; McKinney 2006a; McKinney & Narayan 2007b; Komissarov & McKinney 2007; Penna et al. 2010).

Recent GRMHD simulations of thick disks indicate that the results for the disk (but not the wind-jet, which for us is less important) are roughly independent of the initial field geometry (McKinney & Narayan 2007a,b; Beckwith et al. 2008a). The vector potential we use is the same as in Penna et al. (2010). It is

$$A_{\phi,N} \propto Q^2 \sin\left(\frac{\log(r/S)}{\lambda_{\text{field}}/(2\pi r)}\right) [1 + 0.02(\text{ranc} - 0.5)], \quad (6)$$

with all other  $A_\mu$  initially zero. We use  $Q = (u_g/u_{g,\text{max}} - 0.2)(r/M)^{3/4}$ , and set  $Q = 0$  if either  $r < S$  or  $Q < 0$ . Here  $u_{g,\text{max}}$  is the maximum value of the internal en-

ergy density in the torus. We choose  $S = 22M$  and  $\lambda_{\text{field}}/(2\pi r) = 0.28$ , which gives initial poloidal loops that are roughly isotropic such that they have roughly 1:1 aspect ratio in the poloidal plane. The form of the potential in equation 6 ensures that each additional field loop bundle has opposite polarity. Perturbations are introduced to excite the magneto-rotational instability (MRI). The second term on the right-hand-side (RHS) of equation 6 is a random perturbation: `ranc` is a random number generator for the domain 0 to 1. Random perturbations were introduced in the initial internal energy density in the same way, with an amplitude of 10%. In Penna et al. (2010), it was found that similar simulations with perturbations of 2% and 10% became turbulent at about the same time, the magnetic field energy at that time was negligibly different, and there was no evidence for significant differences in any quantities during inflow equilibrium.

### 3.3. Numerical methods

We perform simulations using a fully 3D version of HARM that uses a conservative shock-capturing Godunov scheme (Gammie et al. 2003; Shafee et al. 2008; McKinney 2006b; Noble et al. 2006; Mignone & McKinney 2007; Tchekhovskoy, McKinney & Narayan 2007; McKinney & Blandford 2009). We use horizon-penetrating Kerr-Schild coordinates for the Kerr metric (Gammie et al. 2003; McKinney & Gammie 2004), which avoids any issues with the coordinate singularity in Boyer-Lindquist coordinates. The code uses uniform internal coordinates  $(t, x^{(1)}, x^{(2)}, x^{(3)})$  mapped to the physical coordinates  $(t, r, \theta, \phi)$ . The radial grid mapping is

$$r(x^{(1)}) = R_0 + \exp(x^{(1)}), \quad (7)$$

which spans from  $R_{\text{in}} = 0.9r_H$  to  $R_{\text{out}} = 200M$ , where  $r_H$  is the radius of the outer event horizon. This just ensures the grid never extends inside the inner horizon, in which case the equations of motion would no longer be hyperbolic. The parameter  $R_0 = 0.3M$  controls the resolution near the horizon. For the outer radial boundary of the box, absorbing (outflow, no inflow allowed) boundary conditions are used.

The  $\theta$ -grid mapping is

$$\theta(x^{(2)}) = \left[ Y(2x^{(2)} - 1) + (1 - Y)(2x^{(2)} - 1)^7 + 1 \right] (\pi/2), \quad (8)$$

where  $x^{(2)}$  ranges from 0 to 1 (i.e. no cut-out at the poles) and  $Y = 0.65$  is chosen to concentrate grid zones toward the equator. Reflecting boundary conditions are used at the polar axes. The  $\phi$ -grid mapping is given by  $\phi(x^{(3)}) = 2\pi x^{(3)}$ , such that  $x^{(3)}$  varies from 0 to 1/2 for a box with  $\Delta\phi = \pi$ . Periodic boundary conditions are used in the  $\phi$ -direction. Penna et al. (2010) considered various  $\Delta\phi$  for thin disks and found little difference in the results. In all of their tests,  $\Delta\phi > 7|h/r|$  and we remain above this limit as well. In what follows, spatial integrals are renormalized to refer to the full  $2\pi$  range in  $\phi$ , even if our computational box size is limited in the  $\phi$ -direction. For the purpose of radiative transfer we combine two identical regions of size  $\Delta\phi = \pi$  preserving the orientation to obtain the span of full  $2\pi$ .

### 3.4. Resolution and Spatial Convergence

The resolution of the simulations is  $N_r \times N_\theta \times N_\phi = 256 \times 64 \times 32$ . This is the fiducial resolution of Penna et al. (2010). Shafee et al. (2008) found this resolution to be sufficient to obtain convergence compared to a similar  $512 \times 128 \times 32$  model. In the vertical direction, we have about 7 grid cells per density scale height. Turbulence is powered by the MRI, which is seeded by the vertical component of the magnetic field (Balbus & Hawley 1998). The characteristic length scale of the MRI is the wavelength of the fastest growing mode:

$$\lambda_{\text{MRI}} = 2\pi \frac{v_A}{\Omega_0}, \quad (9)$$

where  $v_A$  is the Alfvén speed. Assuming hydrostatic equilibrium, we can rewrite this formula near the midplane of the disk in terms of the dimensionless disk thickness  $h/r$  and the plasma  $\beta$ :

$$\lambda_m = 2\pi(h/r) \frac{1}{\sqrt{\beta}} r. \quad (10)$$

Clearly the MRI is most difficult to resolve when  $\beta$  is large. We have local values of  $\beta \sim 20 - 100$  initially and then  $\beta$  decreases until it is order  $\beta \sim 10$  in the disk beyond the black hole and order  $\beta \sim 1$  near the black hole due to the instability exponentially amplifying the initial field. We find that  $\lambda_m > h/r$  always, and the MRI is well-resolved in the midplane of disk both initially and in the saturated state because  $h/r$  is resolved by the chosen  $\theta$  grid. Penna et al. (2010) studied convergence in  $N_r$ ,  $N_\theta$ , and  $N_\phi$  and found that models with  $N_r = 256$  or  $N_r = 512$ ,  $N_\theta = 64$  or  $N_\theta = 128$ , and  $N_\phi = 64$  or  $N_\phi = 32$  behaved similarly for disks with similar resolution across the disk. Our resolution of the MRI and prior convergence testing by Penna et al. (2010) for similarly-resolved disks justify our choice of grid resolution. It is currently not computationally feasible to perform a similar spin parameter study at much higher resolutions, and future studies will continue to explore whether such simulations are fully converged.

A key feature of our code is the use of a 3rd order accurate (4th order error) PPM scheme for the interpolation of primitive quantities (i.e. rest-mass density, 4-velocity relative to a zero angular momentum observer (ZAMO), and lab-frame 3-magnetic field) (McKinney 2006a). Simulations of fully three-dimensional models of accreting black holes producing jets using our 3D GRMHD code show that this PPM scheme leads to an improvement in effective resolution by at least factors of roughly two per dimension as compared to the original HARM MC limiter scheme for models with resolution  $256 \times 128 \times 32$  (McKinney & Blandford 2009). The PPM method is particularly well-suited for resolving turbulent flows since they rarely have strong discontinuities and have most of the turbulent power in long wavelength modes. Even moving discontinuities are much more accurately resolved by PPM than minmod or MC. For example, even without a steepener, a simple moving contact or moving magnetic rotational discontinuity is sharply resolved within about 4 cells using the PPM scheme as compared to being diffusively resolved within about 8-15 cells by the MC limiter scheme.

### 3.5. Ceiling constraints

During the simulation, the rest-mass density and internal energy densities can become quite low beyond the corona, but the code only remains accurate and stable for a finite value of  $b^2/\rho$ ,  $b^2/u_g$ , and  $u_g/\rho$  for any given resolution. We enforce  $b^2/\rho \lesssim 10$ ,  $b^2/u_g \lesssim 100$ , and  $u_g/\rho \lesssim 10$  by injecting a sufficient amount of mass or internal energy into a fixed zero angular momentum observer (ZAMO) frame with 4-velocity  $u_\mu = \{-\alpha, 0, 0, 0\}$ , where  $\alpha = 1/\sqrt{-g^{tt}}$  is the lapse.

We have checked the ceilings are rarely activated in the regions of interest of the flow. Figure 2 shows the constrained ratios,  $b^2/\rho$ ,  $b^2/u_g$ , and  $u_g/\rho$ , as a function of  $\theta$  at six radii ( $r = 4, 6, 8, 10, 12$ , and  $14M$ ) for the  $a_* = 0$  model. The data has been time-averaged over the steady state period from  $t = 14000M$  to  $200000M$ . The ceiling constraints are shown as dashed red lines, and we see that the solution stays well away from the ceilings. This shows that the ceilings are sufficiently high.

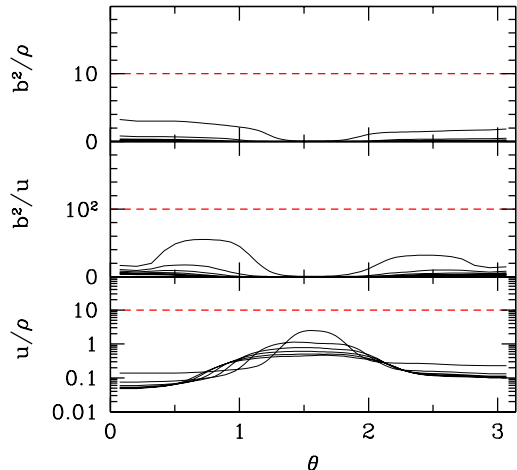


**Figure 2.** Ratios of  $b^2/\rho$ ,  $b^2/u_g$ , and  $u_g/\rho$  versus  $\theta$ . Black curves correspond to different radii in the flow; from top to bottom,  $r = 4, 6, 8, 10, 12$ , and  $14M$ . The data is time-averaged over the steady state period of the flow, from  $t = 14000M$  to  $200000M$ . Numerical ceilings constrain the solution to lie below the dashed red lines, but we see that the solution does not approach these limits.

### 3.6. Temporal Convergence

We run the simulations from  $t = 0M$  to  $t = 20000M$ . The accretion rate, the height- and  $\phi$ -averaged plasma  $\beta$ , and other disk parameters, fluctuate turbulently about their mean values. The simulation reaches a quasi-steady state, when the mean parameter value are time-independent. Figure 3 shows the accretion rate and height- and  $\phi$ -averaged  $\beta$  at the event horizon as a function of time for all five models. We take the period from  $t = 14000M$  to  $t = 20000M$  to define steady state.

As shown in Penna et al. (2010), for disk models like the one considered, the disk outside the innermost stable circular orbit (ISCO) behaves like the  $\alpha$ -disk model with  $\alpha \sim 0.1$  across disk thicknesses of  $h/r \sim 0.05 - 0.4$ . This allows one to accurately infer the timescale for

reaching “inflow equilibrium,” corresponding to a quasi-steady flow across all quantities, at a given radius. For  $h/r \sim 0.3$  by  $t \sim 15000M$ - $20000M$  (the simulation runs till  $20000M$ , but the initial  $5000M$  are transients not necessarily associated with achieving inflow equilibrium for a simple viscous disk), we use the results in Appendix B of Penna et al. (2010) and find that inflow equilibrium is achieved within a radius of  $r \sim 25M$ - $30M$  for models with  $a_* \sim 1$  and  $r \sim 35M$  for models with  $a \sim 0$ . Even for a doubling of the viscous timescale, inflow equilibrium is achieved by  $r \sim 20M$ - $25M$  depending upon the black hole spin. This motivates using an analytical extension of the simulation solution for radii beyond  $r \sim 25M$  as described later in section 4.2.

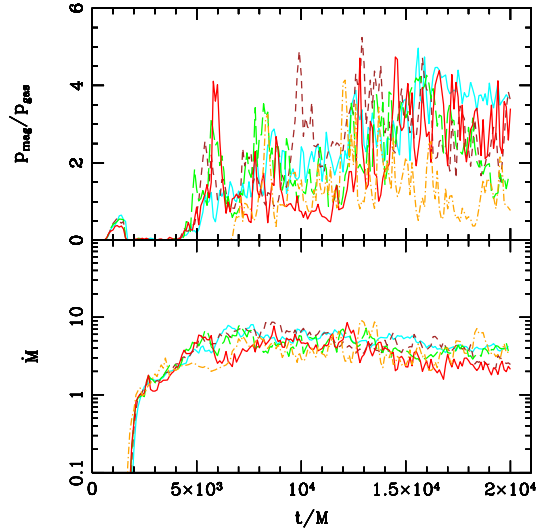


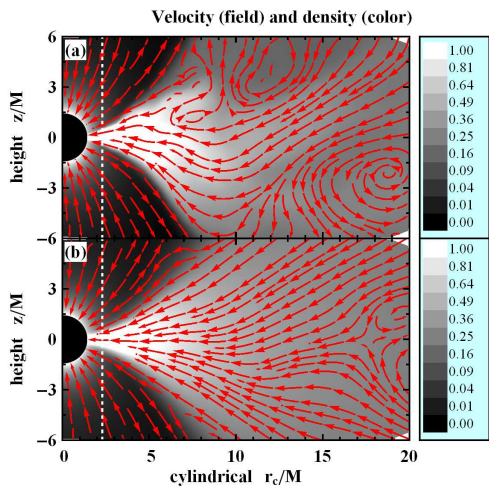
**Figure 3.** Accretion rate and height- and  $\phi$ -averaged  $\beta$  versus time at the event horizon for all five models:  $a_* = 0$  (dotted black),  $a_* = 0.5$  (solid red),  $a_* = 0.7$  (long-dashed green),  $a_* = 0.9$  (short-dashed brown), and  $a_* = 0.98$  (dot-dashed orange).

### 3.7. Evolved disk structure

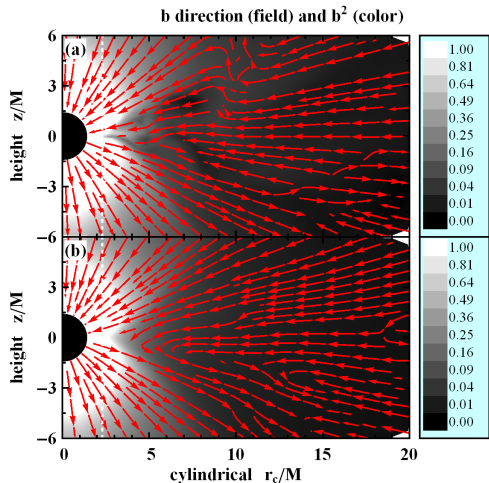
Figure 4 shows matter stream lines as vectors and number density  $n_e$  as greyscale map. The large scale vortices existing on a single time shot (panel (a)) almost disappear, when averaged over  $6000M$  (panel (b)) in between  $14000M$  and  $20000M$ . The density is the highest in the equatorial plane on average, but deviations are present on the instantaneous map. The ISCO does not have any special significance: density and internal energy density increase through ISCO towards the black hole horizon.

Figure 5 shows magnetic field lines as vectors and comoving electromagnetic energy density  $\propto b^2$  as a greyscale map. The structure of magnetic field at early times remembers the initial multi-loop field geometry (Penna et al. 2010), but switches at late times to a helical magnetic field structure resembling a split-monopole in meridional projection. Such switching of magnetic field structure suggests that final helix with projected split monopole is a universal configuration as a natural outcome any vertical flux being dragged into the black hole. The magnetic field structure of a single snapshot (panel (a)) looks quite similar to the structure of the linear average between  $14000M$  and  $20000M$  (panel (b)). The

polar region of the flow has the strongest magnetic field.



**Figure 4.** Stream lines of velocity (red vectors) and number density  $n_e$  (greyscale map) for spin  $a_* = 0.9$  at  $\phi = 0$  in the meridional plane: single timeshot at  $t = 14000M$  on the upper (a) panel and time average between  $t = 14000M$  and  $t = 20000M$  on the lower (b) panel. The correspondent calibration bars of  $n_e$  are shown on the right. Number density is normalized by its maximum value.



**Figure 5.** Magnetic field lines (red vectors) and comoving electromagnetic energy density  $\propto b^2$  (greyscale map) for spin  $a_* = 0.9$  at  $\phi = 0$  in the meridional plane ( $r_c$  as cylindrical radius): single timeshot at  $t = 14000M$  on the upper (a) panel and time average between  $t = 14000M$  and  $t = 20000M$  on the lower (b) panel. The correspondent calibration bars of comoving  $b^2$  are shown on the right. Magnetic field energy density is normalized by its maximum value.

#### 4. AVERAGED DYNAMICAL MODEL

We now discuss the link between the numerical simulations and the averaged dynamical model. We need to decide on the averaging, especially of the magnetic field, extend the simulations to large radii, and define the electron temperature.

##### 4.1. Averaging

We need the time-averaged dynamical model for the purpose of analyzing the whole model parameter space of spin  $a_*$ , inclination angle  $\theta$ , accretion rate  $\dot{M}$ , and ratio of proton to electron temperatures  $T_p/T_e$  computed at  $6M$ . As we will show later, it is not computationally viable to surf this parameter space, so instead average fluxes are computed over the series of simulation snapshots. The average model incorporates temporal averages at each point in the space of number density  $n$ , velocity  $u^\alpha$ , and internal energy density  $u_g$ . There is no unique approach to averaging the magnetic field  $\mathbf{b}$ , the results may depend on the approach employed. We choose one reasonable prescription and test the resultant steady-state dynamical model.

For averaging  $\mathbf{b}$  is computed at each point and at each time in the instantaneous comoving locally flat reference frame. The magnetic field randomly changes orientation in the midplane with time due to turbulence. So, the linear time average would underestimate the magnetic field and would not be independent of averaging period. It is more viable to modify the linear averaged  $\mathbf{b}$  at each point by the value of  $f = \sqrt{\langle b^2 \rangle_t / \langle \mathbf{b} \rangle_t^2}$  computed at that point. Then the dynamical model has an increased field  $\mathbf{b}_{RMS} = f \langle \mathbf{b} \rangle_t$  with a strength typical for a single snapshot, but likely more uniform in direction than  $\mathbf{b}$  in a single snapshot. We call the latter the RMS-field model. We run radiative transfer on the top of each set of dynamical models the RMS-field averaging. To estimate the effect of using the RMS-field model, we compute radiative transfer also for the models with linear-averaged  $\mathbf{b}$ -field. Averaging is done over 200 snapshots during the steady state period between  $t = 14000M$  and  $t = 20000M$ . A detailed comparison of how different averaging methods affect the polarized radiative transfer will be presented in a follow-up paper.

##### 4.2. Extension to large radii

The flow is evolved in a quasi-steady state for  $6000M$  from  $14000M$  until  $20000M$ , which corresponds to 8 orbits at  $r = 25M$ . The flow is not sufficiently settled at larger radii, however, some Faraday rotation might happen and some emission might occur outside  $25M$ . Thus, we extend the dynamical model to larger radii  $r > 25M$  in a reasonable way and check in Appendix A how much the various extensions change the results of radiative transfer. The boundary of radiative transfer is situated at  $r = 20000M$ . The profiles of number density  $n_e$ , internal energy density  $u_g$ , magnetic field  $\mathbf{b}$  and velocity  $\mathbf{v}$  are extended as power-laws until radius  $r = 20000M$ . The relevant power-law  $\beta$  is obtained for number density by matching the known value  $n_e = 130\text{cm}^{-3}$  at about  $1.5'' \approx 3 \cdot 10^5 M$  (Baganoff et al. 2003) and the average  $n_{e,\text{cut}}$  value at  $r = 25M$  in the equatorial plane for each model. The value of  $\beta$  may be different for different models. The radial flow velocity  $v_r$  is then obtained from the continuity relation in the equatorial plane  $n_e v_r r^2 = \text{const}$ . The power-law of internal energy density  $u_g$  is obtained in a similar way by matching the values  $T_e = T_p = 1.5 \cdot 10^7$  K and  $n_e = 130\text{cm}^{-3}$  at  $3 \cdot 10^5 M$  (Baganoff et al. 2003; Shcherbakov & Baganoff 2010). The extensions of other flow velocities and magnetic field are fixed in turn. The meridional physical velocity is extended as  $v_\theta \propto (r/M)^{-3/2}$ , toroidal as



$v_{\hat{\phi}} \propto (r/M)^{-1/2}$ , where the relationship  $v_i \approx u^i \sqrt{g_{ii}}$  is used to connect the 4-velocity components with physical velocity components. All components of comoving magnetic field are extended as  $b_r, b_\theta, b_\phi \propto (r/M)^{-3/2}$ . This power-law slope is similar to the one observed in the simulations between  $15M$  and  $25M$ . However, this choice will likely underestimate the magnetic field at large radii, since the slope is shallower for equipartition assumption  $b \propto \sqrt{nT_p} \propto (r/M)^{-1}$  for  $n \propto (r/M)^{-1}$ . Exploration of various extensions of the magnetic field will be the topic of future studies.

After defining the extension power-laws for quantities in the equatorial plane, we extend the quantities radially at arbitrary  $\theta$  and  $\phi$  in a continuous way. For example, for density at arbitrary  $\theta$  and  $\phi$  and  $r > 25M$  we have

$$n_e(r, \theta, \phi) = n_e(25M, \theta, \phi) \left( \frac{r}{25M} \right)^{-\beta}, \quad (11)$$

where  $n_e(25M, \theta, \phi)$  is taken from the simulation. We similarly extend other quantities. As we will show in Appendix A, reasonable variations in power-law indices bear minimum influence on radiation intensities, linear and circular polarization fluxes.

#### 4.3. Electron temperature

Neither the proton  $T_p$  nor electron  $T_e$  temperatures are given directly by the simulation. However, it is crucial to know the electron temperature  $T_e$  to determine the emission. Our solution is to split the total internal energy density  $u_g$ , given by the simulation and power-law extension, between the proton energy and the electron energy. The energy balance states

$$\frac{u_g}{\rho} \equiv \frac{u_{p,g} + u_{e,g}}{\rho} = c_p k_B T_p + c_e k_B T_e, \quad (12)$$

where  $c_p = 3/2$  and  $c_e \geq 3/2$  are the respective heat capacities,  $\rho$  is the rest-mass density, and  $k_B$  is Boltzmann's constant. The difference of temperatures  $T_p - T_e$  is influenced by three effects: equilibration by Coulomb collisions at large radii, the difference in heating rates  $f_p$  and  $f_e$  of protons and electrons operating at intermediate radii, and the difference in heat capacities operating close to the BH. The effect of radiative cooling is excluded from the list, since, according to Sharma et al. (2007), the radiative efficiency of the flow is negligible for realistic  $\dot{M} \lesssim 10^{-7} M_\odot \text{year}^{-1}$ . The aforementioned important effects can be incorporated into an equation as

$$v_r \frac{d(T_p - T_e)}{dr} = -\nu_c (T_p - T_e) + \left( \frac{1}{c_p} \frac{f_p}{f_p + f_e} - \frac{1}{c'_e} \frac{f_e}{f_p + f_e} \right) v_r \frac{d(u_g/\rho)}{k_B dr}, \quad (13)$$

where

$$\nu_c = 8.9 \cdot 10^{-11} \left( \frac{T_e}{3 \cdot 10^{10}} \right)^{-3/2} \frac{n_e}{10^7} \quad (14)$$

is the non-relativistic temperature equilibration rate by collisions (Shkarofsky et al. 1966), all quantities being measured in CGS units. We consider protons to always have non-relativistic heat capacity and collisions to always obey the non-relativistic formula. The magnitudes

of errors introduced by these simplification are negligible. The exact expressions for total electron heat capacity and differential heat capacity are approximated as

$$c_e = \frac{u_{e,g}/\rho}{k_B T_e} \approx \frac{3}{2} \frac{0.7 + 2\theta_e}{0.7 + \theta_e}, \quad (15)$$

$$c'_e = \frac{d(u_{e,g}/\rho)}{k_B dT_e} \approx 3 - \frac{0.735}{(0.7 + \theta_e)^2} \quad (16)$$

correspondingly with the error  $< 1.3\%$ , where

$$\theta_e = \frac{k_B T_e}{m_e c^2} \quad (17)$$

is the dimensionless electron temperature. It was recently shown (Sharma et al. 2007) that the ratio of heating rates in the non-relativistic regime in a disk can be approximated as

$$\frac{f_e}{f_p} = C \sqrt{\frac{T_e}{T_p}} \quad (18)$$

with a constant  $C$ . This formula is adopted in the relativistic regime as well, since no better prescription is available. Sharma et al. (2007) found the value  $C = 0.33$  in simulations, whereas we find  $C = 0.40 - 0.45$  for the best-fitting models (see § 7). The proton and electron temperatures are determined at each point in the following way. We first take an averaged model (see Subsection 4.2) of a simulation with spin  $a_*$  extended to  $r = 20000M$ . Then we compute azimuthal averages of radial velocity  $v_r$ , number density  $n_e$ , and  $u_g/\rho$  at the equatorial plane, extend them as power laws to  $r_{\text{out}} = 3 \cdot 10^5 M$ , and solve the equations (12,13) from  $r_{\text{out}}$  down to the inner grid cell point. Temperatures are set to  $T_e = T_p = 1.5 \cdot 10^7$  K at  $r_{\text{out}}$  (Baganoff et al. 2003; Shcherbakov & Baganoff 2010). On the next step we make a correspondence of the values of  $u_g/\rho$  to the calculated  $T_e$  and  $T_p$  and define functional dependence  $T_e = T_e(u_g/\rho)$  and  $T_p = T_p(u_g/\rho)$ . At each point of the simulation (including off the equator), we draw temperatures from this correspondence. Typical profiles of proton and electron temperatures are shown on Figure 6. Temperatures stay equal until  $\sim 10^4 M$  due to collisions despite different heating prescriptions. Within  $3 \cdot 10^3 M$  the timescale of collisional equilibration becomes relatively long and electrons become relativistic, thus  $T_e$  drops down below  $T_p$ . We take the inner part within  $r < 20000M$  of the electron and proton temperature profiles to conduct the radiative transfer.

For a given accretion rate there exists a unique dependence of the ratio of temperatures  $T_p/T_e$  at  $6M$  on the heating constant  $C$ . Thus, we interchangeably refer to the ratio of temperatures  $T_p/T_e$  at  $6M$  or the correspondent heating constant  $C$ . We commonly use the ratio of temperatures as a more straightforward quantity.

## 5. GENERAL RELATIVISTIC POLARIZED RADIATIVE TRANSFER

General relativistic polarized radiative transfer is an essential tool for converting the dynamical model of an accretion flow into a set of observable quantities (Broderick et al. 2009; Gammie & Leung 2010; Shcherbakov & Huang 2011). We closely follow Shcherbakov & Huang (2011) for the transfer technique.

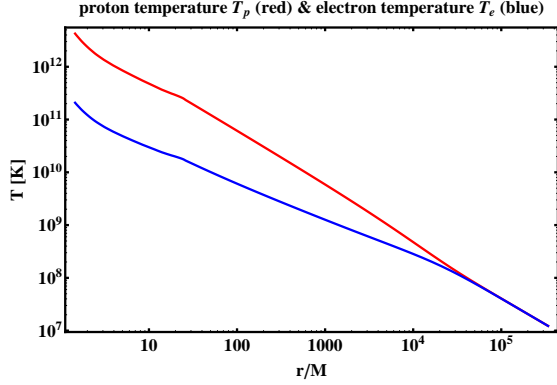


**Figure 6.** Temperatures of protons  $T_p$  (upper red line) and electrons  $T_e$  (lower blue line) as functions of radius for heating parameter  $C = 0.414$  and accretion rate  $\dot{M} = 1.04 \times 10^{-8} M_\odot \text{year}^{-1}$ , which leads to  $T_p/T_e = 17.6$  and  $T_e = 4.2 \cdot 10^{10}$  K at  $r = 6M$ . The dynamic RMS-field model with this heating prescription, this accretion rate, and spin  $a_* = 0.9$  provides the fit with the lowest  $\chi^2$  to polarization observations (see § 7).

Similarly to Huang et al. (2009a), we define the polarized basis in the picture plane, where one vector points North, another vector points East, and the wavevector points towards the observer. We parallel transport this basis in the direction of the black hole and do the radiative transfer along the ray in the opposite direction. At each point along the ray we go to the locally-flat comoving frame, calculate the angles between the magnetic field and basis vectors, and compute the Faraday conversion, Faraday rotation, emissivities, and absorptivities. This approach appears no harder computationally compared to the covariant calculation of angles without the locally flat comoving frame (Broderick et al. 2009; Huang et al. 2009a).

Only our calculations of plasma response is different from Shcherbakov & Huang (2011). That paper offered a way to find exact emissivities, absorptivities, Faraday rotation, and conversion coefficients for thermal and other isotropic particle distributions. Here, for simplicity, we employ fitting formulas for Faraday rotation and Faraday conversion and synchrotron approximation for emissivities in thermal plasma. We define

$$X = \frac{2}{3} \frac{\nu}{\nu_B \gamma^2 \sin \theta_B}, \quad (19)$$

where  $\theta_B$  is  $\mathbf{k}\text{-}\mathbf{b}$  angle,  $\gamma$  is electron gamma factor, and  $\nu_B = eb/(2\pi m_e c)$  is the cyclotron frequency. Then following Legg & Westfold (1968); Melrose (1971), we write down emissivities in I, Q, and V modes as

$$\begin{aligned} \varepsilon_I &= \frac{\sqrt{3}}{2} \frac{e^2}{c} \nu_B \sin \theta_B \int_1^{+\infty} d\gamma N(\gamma) X \int_X^{+\infty} dz K_{5/3}(z), \\ \varepsilon_Q &= \frac{\sqrt{3}}{2} \frac{e^2}{c} \nu_B \sin \theta_B \int_1^{+\infty} d\gamma N(\gamma) X K_{2/3}(X), \\ \varepsilon_V &= \frac{2}{\sqrt{3}} \frac{e^2}{c} \nu_B \cos \theta_B \int_1^{+\infty} d\gamma \frac{N(\gamma)}{\gamma} \times \\ &\quad \times \left[ X K_{1/3}(X) + \int_X^{+\infty} dz K_{1/3}(z) \right]. \end{aligned} \quad (20)$$

Here  $K_z(x)$  is the Bessel function of the 2nd kind of or-

der  $z$ . We employed IEEE/IAU definitions of Stokes  $Q$ ,  $U$ , and  $V$  (Hamaker & Bregman 1996), also chosen in Shcherbakov & Huang (2011): counter-clockwise rotation of electric field as seen by the observer corresponds to positive  $V > 0$ . Under this definition the sign of  $V$  emissivity (20) is opposite that in standard theoretical textbooks (Rybicki & Lightman 1967). A variation of emissivity formulas (19,20) exists: Sazonov (1969); Pacholczyk (1970) effectively define  $X = 2\nu/(3\nu_B(\gamma - 1)^2 \sin \theta_B)$ , integrating over particle energy instead of  $\gamma$ . This approximation appears to give significantly larger errors at low particle energies.

Next, one needs to specify, which particle distribution  $N(\gamma)$  to use. Various  $N(\gamma)$  correspond to several synchrotron approximations for thermal plasmas. The ultrarelativistic approximation (Pacholczyk 1970; Huang et al. 2009a) with  $N(\gamma) = \exp(-(\gamma - 1)/\theta_e)(\gamma - 1)^2/2/\theta_e^3$  gives the simplest distribution. However, the exact thermal distribution of particles

$$N(\gamma) = \gamma \sqrt{\gamma^2 - 1} \frac{\exp(-\gamma/\theta_e)}{\theta_e K_2(\theta_e^{-1})} \quad (21)$$

allows for more precise computation of radiation. Synchrotron emissivities based on the equations (19,20) with the exact thermal distribution (21) agree with the exact cyclo-synchrotron emissivities  $\varepsilon_I$ ,  $\varepsilon_Q$ , and  $\varepsilon_V$  (Leung, Gammie & Noble 2009; Shcherbakov & Huang 2011) to within 2% for typical dynamical models and frequencies  $> 100$  GHz. Emissivities integrated over the ultrarelativistic thermal distribution normally have  $\sim 10\%$  error.

Thermal absorptivities are found from emissivities (20) via Kirchhoff's law

$$\alpha_{I,Q,V} = \varepsilon_{I,Q,V}/B_\nu, \quad (22)$$

where  $B_\nu = 2k_B T_e \nu^2/c^2$  is the source function for low photon energies  $h\nu \ll k_B T_e$ . Faraday rotation  $\rho_V$  and Faraday conversion  $\rho_Q$  coefficients are taken from Shcherbakov (2008):

$$\begin{aligned} \rho_V &= g(Z) \frac{2n_e e^2 \nu_B}{m_e c \nu^2} \frac{K_0(\theta_e^{-1})}{K_2(\theta_e^{-1})} \cos \theta, \\ \rho_Q &= f(Z) \frac{n_e e^2 \nu_B^2}{m_e c \nu^3} \left[ \frac{K_1(\theta_e^{-1})}{K_2(\theta_e^{-1})} + 6\theta_e \right] \sin^2 \theta. \end{aligned} \quad (23)$$

Here

$$Z = \theta_e \sqrt{\sqrt{2} \sin \theta \left( 10^3 \frac{\nu_B}{\nu} \right)} \quad (24)$$

and

$$\begin{aligned} g(Z) &= 1 - 0.11 \ln(1 + 0.035Z), \\ f(Z) &= 2.011 \exp\left(-\frac{Z^{1.035}}{4.7}\right) - \\ &\quad - \cos\left(\frac{Z}{2}\right) \exp\left(-\frac{Z^{1.2}}{2.73}\right) - 0.011 \exp\left(-\frac{Z}{47.2}\right) \end{aligned} \quad (25)$$

are the fitting formulas for deviations of  $\rho_V$  and  $\rho_Q$  from analytic results for finite ratios  $\nu_B/\nu$ . The deviation of  $f(Z)$  from 1 is significant for the set of observed frequencies  $\nu$ , temperatures  $\theta_e$ , and magnetic fields found in the typical models of Sgr A\*. These formulas constitute a

good fit to the exact result for the typical parameters of the dynamical model (Shcherbakov 2008).

With all the sophisticated physics incorporated into the radiative transfer, the speed of the numerical code becomes an essential constraint. Polarized radiative transfer can take much longer to perform compared to non-polarized radiative transfer when using an explicit integration scheme to evolve the Stokes occupation numbers  $N_Q$ ,  $N_U$ , and  $N_V$ . Large Faraday rotation measure and Faraday conversion measure lead to oscillations between occupation numbers. One of the solutions is to use an implicit integration scheme, while another solution is to perform a substitution of variables. In the simple case of Faraday rotation leading to interchange of  $N_Q$  and  $N_U$ , the obvious choice of variables is the amplitude of oscillations and the phase. Thus the cylindrical polarized coordinates arise

$$\begin{aligned} N_Q &= N_{QU} \cos \phi, \\ N_U &= N_{QU} \sin \phi. \end{aligned} \quad (26)$$

Then the amplitude  $N_{QU}$  slowly changes along the ray and the angle  $\phi$  changes linearly, which gives an improvement in speed. In the presence of substantial Faraday conversion, the polarization vector precesses along some axis in Poincaré sphere, adding an interchange of circularly and linearly polarized light. Polar polarized coordinates would be more suitable in this case:

$$\begin{aligned} N_Q &= N_{\text{pol}} \cos \phi \sin \psi, \\ N_U &= N_{\text{pol}} \sin \phi \sin \psi, \\ N_V &= N_{\text{pol}} \cos \psi, \end{aligned} \quad (27)$$

where  $N_{\text{pol}}$  is the total polarized intensity, the change of  $\phi$  angle is mainly due to Faraday rotation and  $\psi$  angle changes owing to Faraday conversion. The application of this technique speeds up the code exponentially at low frequencies  $\nu < 100$  GHz.

Besides improving the speed, we perform a number of convergence tests to make sure the final intensities are precisely computed. Radiative transfer involves shooting a uniform grid of  $N \times N$  geodesics from the picture plane. Even though  $N = 150$  (Dexter et al. 2009) maybe a better number to use for a single snapshot,  $N = 111$  works well for the averaged smooth flow giving an accuracy of  $\Delta(\chi^2/\text{dof}) \leq 0.02$  near best-fitting models. The metrics of relative integration error  $\chi_H^2/\text{dof}$  is defined in Appendix A, where the convergence tests are described. The size of the integration domain is taken to be a square in the picture plane with a side

$$a[M] = 16 + 2 \left( \frac{600}{\nu[\text{GHz}]} \right)^{1.5} \quad (28)$$

in the units of  $r_g \equiv M$ , where frequency  $\nu$  is in GHz. The size based on formula (28) is larger than the photon orbit visible diameter  $d_{\text{ph}} \approx 10.4M$  at the same time following the intrinsic size dependence on frequency (Shen et al. 2005; Doeleman et al. 2008) at low frequencies. Justification of this size by convergence tests is given in Appendix A. A surprisingly important radiative transfer parameter is the distance from the BH, where intensity integration starts. The dependence of synchrotron emissivity on temperature and magnetic field strength is so strong that it negates the effect of gravitational redshift

close to the BH. The accuracy of  $\Delta(\chi^2/\text{dof}) \leq 0.02$  is achieved in sub-mm for computation out from  $r_{\text{min}} = 1.01r_H$ , where  $r_H = M(1 + \sqrt{1 - a_*^2})$  is the horizon radius. Higher  $r_{\text{min}}$  leads to larger error  $\Delta(\chi^2/\text{dof}) \sim 0.03$  (see Appendix A).

## 6. STATISTICAL ANALYSIS

Statistical analysis is a necessary tool to compare the model predictions to observations and to discriminate between models. However, it has only recently been applied to the accretion flow in the Galactic Center (Dexter et al. 2009; Broderick et al. 2009; Shcherbakov & Baganoff 2010). When the number of model parameters is large (Huang et al. 2009a) or the number of considered observations is small (Moscibrodzka et al. 2009), it is possible to find an exact fit to the data or say that for some model parameters the fit does not exist. Instead, we consider a broad range of observations and explore models with only 4 parameters: spin  $a_*$ , inclination angle  $\theta$ , accretion rate  $\dot{M}$ , ratio of proton to electron temperature  $T_p/T_e$  at  $6M$ .

We have proven in Section 2 that samples of total fluxes, log LP and EVPA at each frequency are consistent with a Gaussian distribution. Thus, we can directly apply  $\chi^2$  statistics. We are comparing means of observed variable fluxes to fluxes computed for the averaged simulation models. We leave the comparison of the observed samples to the samples generated over many snapshots to future work. We define  $\chi_F^2$  for flux fitting as

$$\chi_F^2 = \sum_{i=1}^7 \frac{(F_{i,\text{sim}} - F_{i,\text{obs}})^2}{\sigma(F)^2}, \quad (29)$$

for the set of 7 frequencies  $\nu = 88, 102, 145, 230, 349, 680,$  and  $857$  GHz, where  $\sigma_F$  are the errors of the means. We add LP fraction at 88, 230, and 349 GHz and CP fraction at 230 and 349 GHz into the full  $\chi^2$ :

$$\begin{aligned} \chi^2 &= \chi_F^2 + \sum_{i=1}^3 \frac{(\log(\text{LP}_{i,\text{sim}}) - \log(\text{LP}_{i,\text{obs}}))^2}{\sigma(\log(\text{LP}))^2} \\ &+ \sum_{i=1}^2 \frac{(\text{CP}_{i,\text{sim}} - \text{CP}_{i,\text{obs}})^2}{\sigma(\text{CP})^2}. \end{aligned} \quad (30)$$

Then we take the number of degrees of freedom to be  $\text{dof}_F = 7 - 3 = 4$  for flux fitting and  $\text{dof} = 12 - 3 = 9$  for fitting all polarized data. We compute the probability density  $\rho(\chi^2) = \rho(\chi^2|a_*, \theta, \dot{M}, C)$  of the data, given a model, from the correspondent  $\chi^2$  distributions. This is a function of spin, inclination angle, accretion rate, and heating constant. Now the search for minimum  $\chi^2$  is fully defined. The probability density of model given data  $\rho(a_*, \theta, \dot{M}, C|\chi^2)$  is needed for confidence intervals calculation. It is found by Bayes' theorem with the use of priors (Broderick et al. 2009)

$$\rho(a_*, \theta, \dot{M}, C|\chi^2) = \frac{\rho(\chi^2)\pi(\theta)\pi(a_*)\pi(\dot{M})\pi(C)}{\int \rho(\chi^2)\pi(\theta)\pi(a_*)\pi(\dot{M})\pi(C)d\theta da_* d\dot{M} dC}, \quad (31)$$

where we assumed a separable prior  $\pi(\theta, a_*, \dot{M}, C) = \pi(\theta)\pi(a_*)\pi(\dot{M})\pi(C)$ . We expect no preferred spin orientation, which requires a uniform distribution over

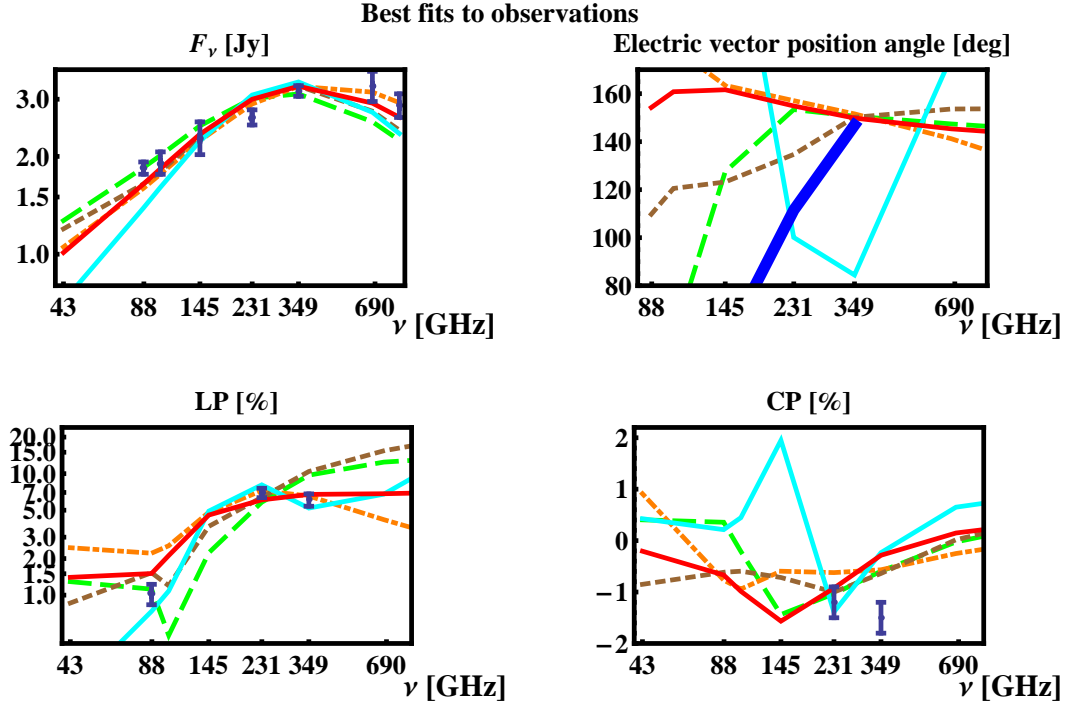


**Figure 7.** Best fits to the observed fluxes, LP and CP fractions by best RMS-field models for each spin. The inclination angle  $\theta$ , accretion rate  $\dot{M}$ , ratio of temperatures  $T_p/T_e$  were adjusted for each spin to minimize  $\chi^2$ . Fits to total flux  $F$  are in the upper left panel, LP fraction in the lower left, and CP fraction in the lower right. Best RMS-field model with spin  $a_* = 0.9$  (solid dark red) has  $\chi^2/\text{dof} = 4.05$ , spin  $a_* = 0.7$  (long-dashed green) —  $\chi^2/\text{dof} = 5.37$ , spin  $a_* = 0.5$  (short-dashed brown) —  $\chi^2/\text{dof} = 5.77$ , spin  $a_* = 0$  (solid light cyan) —  $\chi^2/\text{dof} = 9.03$ , spin  $a_* = 0.98$  (dot-dashed orange) —  $\chi^2/\text{dof} = 4.85$ . The upper left panel shows the dependence of EVPA angle on frequency for the best models. Note, that EVPA angles are not included into our  $\chi^2$  fitting procedure. The thick blue curve represents observations. Simulated EVPA curves are arbitrarily shifted to approximate EVPA at 349 GHz. The addition of an external (to the emitting region) Faraday rotation screen helps to fit EVPA(349 GHz) – EVPA(230 GHz).

the solid angle and the prior  $\pi(\theta) = \sin\theta$ . Following Broderick et al. (2009) we take a uniform prior on spin  $\pi(a_*) = 1$ . The accretion rate  $\dot{M}$  is largely uncertain. For our analysis we take the logarithmic prior  $\pi(\dot{M}) = \dot{M}^{-1}$ , which is the best non-informative prior for large range of possible values (Jaynes & Bretthorst 2003). The value of the heating constant  $C = 0.33$  cited by Sharma et al. (2007) was based on only a small part of total energy dissipation and may be unreliable. A similar prior  $\pi(C) = C^{-1}$  can be taken for the heating constant. The expectation value of any quantity  $Q$  at certain spin  $a_*$  is calculated as the integral

$$\langle Q_{a_*} \rangle = \iiint Q \rho(a_*, \theta, \dot{M}, C | \chi^2) \sin\theta d\theta \frac{dC}{C} \frac{d\dot{M}}{\dot{M}}, \quad (32)$$

and the confidence intervals are found analogously.

We explore the values of  $C$  from 0.20 to 0.75, which leads to  $T_p/T_e$  at  $6M$  between 6 and 60. All models fitting  $F_\nu$  SED with  $C = 0.20$  underpredict the linear polarization and all models with  $C = 0.75$  overpredict the linear polarization, thus we cover all good models by using a wide range of  $C$ . A full analysis in the space of accretion rate  $\dot{M}$  is not possible due to limited computational resources. Instead, for each spin  $a_*$ , heating constant  $C$ , and inclination  $\theta$  we find the best  $\chi^2_F$  for the values of flux  $F_\nu$  (see eq.29) and explore the region close to the best fit. As the dependence of flux on accretion rate is uniform, this guarantees that we explore all regions with good full  $\chi^2$  defined by equation (30). Even

if there is some good fit to LP and CP curves, but the flux values are either overpredicted or underpredicted, then the total  $\chi^2/\text{dof}$  would be substantially larger than unity.

## 7. RESULTS

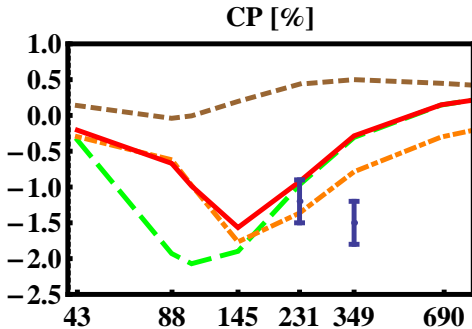
In previous sections we described observations, numerical simulations of the dynamical structure, averaged model, polarized radiative transfer, and statistical methods to compare the simulated spectra with the observations. Now we are ready to present the results of such a comparison, done for the first time for GR polarized radiative transfer over the model derived from 3D GRMHD simulations. We are able to achieve  $\chi^2/\text{dof} \sim 4$  fits to observations and constrain some model parameters.

Figure 7 shows best fits to observations by RMS-field (RMS magnetic field strength, mean direction) models with five different spins. Inclination angle  $\theta$ , accretion rate  $\dot{M}$ , heating constant  $C$  were adjusted to reach the lowest  $\chi^2$ . The best RMS-field model with spin  $a_* = 0.9$  (solid dark red) has  $\chi^2/\text{dof} = 4.05$ , spin  $a_* = 0.7$  (long-dashed green) —  $\chi^2/\text{dof} = 5.37$ , spin  $a_* = 0.5$  (short-dashed brown) —  $\chi^2/\text{dof} = 5.77$ , spin  $a_* = 0$  (solid light cyan) —  $\chi^2/\text{dof} = 9.03$ , spin  $a_* = 0.98$  (dot-dashed orange) —  $\chi^2/\text{dof} = 4.85$ . Let us discuss how well the models with different spins perform. Fits to fluxes  $F_\nu$  on upper left are not substantially different, though models with higher spins perform better at both low and high frequencies. Larger deviations can be seen on LP (lower

left) and CP (lower right) plots. Models with high spins require lower accretion rate/density to fit the flux spectrum. Then they are not subject to Faraday depolarization, which leads to decrease of LP at low  $\nu$ , and the models end up having larger linear polarization fractions at 88 GHz. Not all models reproduce the observed decrease of mean LP fraction between 231 GHz and 349 GHz groups. The discrepancies in fitting CP fraction are also large: no low- $\chi^2$  model can reproduce CP = -1.5% at 349 GHz: best RMS-field models have  $|CP| < 1\%$  at this frequency. However, only low spin solutions reproduce the correct sign and the order of magnitude of difference between EVPA(349 GHz) and EVPA(230 GHz), whereas the models with higher spin have shallower difference of the opposite sign EVPA(349 GHz) - EVPA(230 GHz) < 0.

The best RMS-field model with spin  $a_* = 0.9$  has inclination angle  $\theta = 52^\circ$ , position angle PA =  $121^\circ \pm 20^\circ$ , accretion rate  $\dot{M} = 1.04 \times 10^{-8} M_\odot \text{year}^{-1}$ , ratio of temperatures  $T_p/T_e = 17.6$  at  $6M$ , which gives  $T_e = 4.2 \cdot 10^{10}$  K at that distance from the center in equatorial plane. In turn, spin  $a_* = 0.9$  model with linear-averaged  $\mathbf{b}$  reaches minimum  $\chi^2/\text{dof} = 5.56$  at  $\theta = 55^\circ$ ,  $\dot{M} = 1.5 \times 10^{-8} M_\odot \text{year}^{-1}$ ,  $T_e = 3.0 \cdot 10^{10}$  K at  $6M$ . Thus, the best linear-averaged model with same spin  $a_* = 0.9$  has 1.5 times larger accretion rate compared to RMS-field model, but also has 1.4 times lower electron temperature. The best RMS-field model is more edge-on.

Let us now separate the physical effects responsible for the observed polarized quantities. Several com-



**Figure 8.** Contributions of different effects to CP fraction dependence on frequency for best-fitting  $a_* = 0.9$  model. Shown are observations (blue error bars), the best fit model (solid red line), the same dynamical model computed with zero V emissivity  $\varepsilon_V = 0$  in radiative transfer so that CP is produced by Faraday conversion (long-dashed green), the same model with zero Faraday conversion  $\rho_Q = 0$  (short-dashed brown), and the same model without Faraday rotation  $\rho_V = 0$  (dot-dashed orange). Emissivity in circular V mode contributes little to the observed CP. Surprisingly, CP does not change sign as a function of frequency. The combined action of Faraday rotation and Faraday conversion takes places around  $\nu = 145$  GHz, the sign of  $V$  changes without Faraday rotation at that frequency.

parably strong radiative transfer effects may account for observed polarized fluxes. Let us consider the production of circular polarization in the flow. Figure 8 shows the consequences of switching various physical effects off for the best-fitting RMS-field model with spin  $a_* = 0.9$ . The solid curve is the result with all physics on. The long-dashed line below is produced, when circular emissivity is

set to  $\varepsilon_V = 0$ . The short-dashed line corresponds to zero Faraday conversion ( $\rho_Q = 0$ ). The changes for the emissivity switched off are small, whereas setting Faraday conversion to zero leads to several times smaller CP of different sign, thus most of CP in this model is produced by Faraday conversion. It would be incorrect, however, to think that the simple linear to circular conversion explains the observed CP. The dot-dashed line in Figure 8 shows the CP fraction, when Faraday rotation is switched off ( $\rho_V = 0$ ). The effect of Faraday rotation is insignificant at  $\nu < 150$  GHz, but the rotation of the plane of linear polarization simultaneous with conversion between linear and circular polarizations produces a unique effect at higher  $\nu$ . This is the so-called “rotation-induced conversion” (Homan et al. 2009). The expected sign oscillations of  $V$  with frequency do not happen, whether or not Faraday rotation is involved. The best spin  $a_* = 0.9$  model exhibits qualitatively similar variations in CP.

On Figure 9 we illustrate the influence of Faraday rotation on LP fraction (left panel) and EVPA angle (right panel). The solid curves have all physics on for the best RMS-field model with spin  $a_* = 0.9$ . The dashed lines are computed for switched off Faraday rotation ( $\rho_V = 0$ ). The Faraday rotation is negligible at high frequencies and curves coincide at  $\nu > 400$  GHz. As the rotation of polarization plane is much stronger at low  $\nu$ , a significant phase shift accumulates between different rays at the low end of the spectrum and cancellations of LP become strong at  $\nu < 150$  GHz. Thus we illustrate the effect of Faraday depolarization (Bower et al. 1999a). In the absence of Faraday rotation the dependence of EVPA on frequency is not a constant line: the variations of intrinsic emitted EVPA are significant. Thus, the change of EVPA with  $\nu$  should not always be ascribed to the effect of Faraday rotation. The positive observed slope of EVPA with  $\nu$ , acquired due to negative Faraday rotation  $\rho_V$ , is comparable to the slope of intrinsic emitted EVPA. The dot-dashed lines correspond to the model, where Faraday rotation is artificially increased 10 times. The model is able to fit EVPA curve, but suffers substantial beam depolarization and underpredicts LP at low frequencies.

Besides computing the best fit models, we examine regions of parameter space near those best fits in search for anomalies. For example, if there is a coincidental cancellation in one of the models, then the close-by models have much higher  $\chi^2/\text{dof}$  and such a best fit may be unreliable as it is accidental. On the Figure 10 we plot contours of  $\chi^2/\text{dof}$  near best-fitting RMS-field model with spin  $a_* = 0.9$  (left column) and linear-averaged spin  $a_* = 0.9$  model (right column) in the space of ratio of temperatures  $T_p/T_e$  at  $6M$  and accretion rate  $\dot{M}$ . The contours of  $\chi^2/\text{dof}$  are color-coded from highest (red) to lowest (blue) values. The upper row shows  $\chi_F^2/\text{dof}_F$  for flux  $F_\nu$  fitting, whereas the lower row shows the full  $\chi^2/\text{dof}$ . Plots of  $\chi_F^2/\text{dof}_F$  (panels (a) and (c)) reveal significant degeneracy between the electron temperature and accretion rate: lower  $T_e$  and higher  $\dot{M}$  or higher  $T_e$  and lower  $\dot{M}$  both fit the flux quite well. The degeneracy breaks for the full  $\chi^2/\text{dof}$ , when fitting LP and CP, which fixes the matter density. The well-fitting phase volume in the parameters of  $T_p/T_e$  and  $\dot{M}$  appears to be similar for both

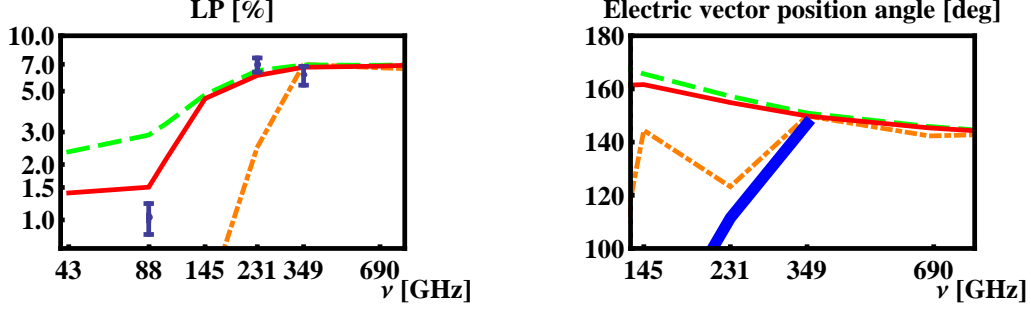


**Figure 9.** Contributions of different effects to LP fraction (on the left) and EVPA angle (on the right) dependencies on frequency for the best-fitting RMS-field  $a_* = 0.9$  model. Shown are observations (blue error bars and thick blue line), the best fit model (solid red line), the same dynamical model computed without Faraday rotation  $\rho_V = 0$  in radiative transfer (long-dashed green), and the same dynamical model with 10 times stronger Faraday rotation  $\rho'_V = 10\rho_V$ . Beam depolarization is weak without Faraday rotation and LP stays high at low frequencies. The change of the EVPA due to Faraday rotation is comparable to the difference of intrinsic emission on EVPA, but has the opposite sign. The best-fitting model with spin  $a_* = 0.9$  has about 10 times lower than observed Faraday rotation.

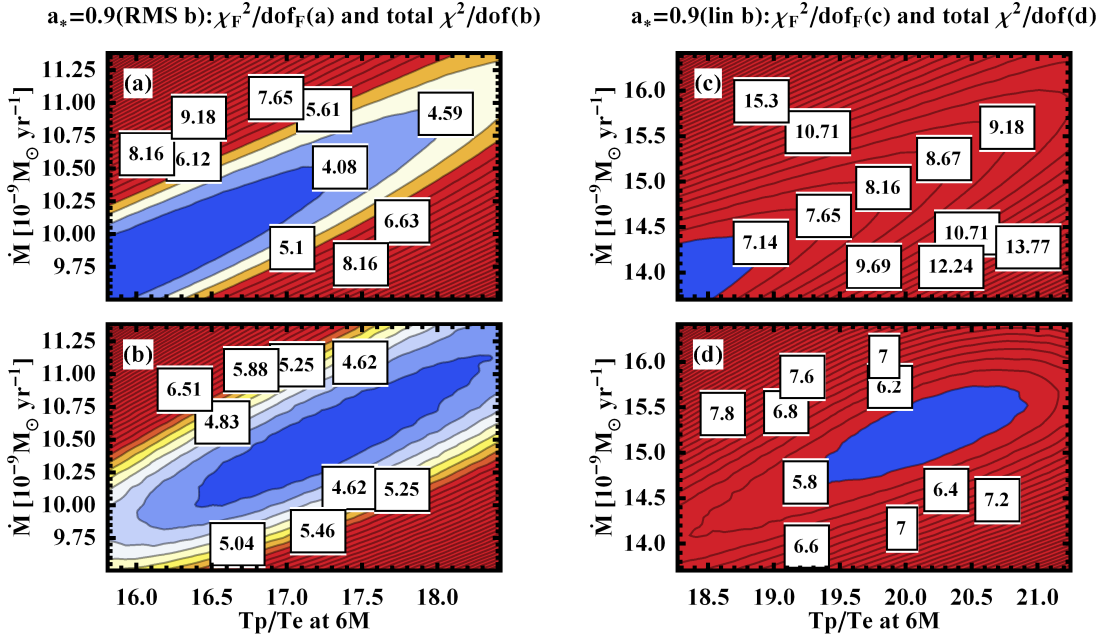


**Figure 10.** Behavior of  $\chi^2$  near the best-fitting models with spin  $a_* = 0.9$ : RMS-field model with RMS-strength magnetic field **b** (left column) and model with linear averaged **b** (right column) with changing accretion rate  $\dot{M}$  and ratio of temperatures  $T_p/T_e$  at  $6M$ . Contours of  $\chi^2_F/dof_F$  for flux fitting are in the upper row, contours for full  $\chi^2/dof$  are in the lower row.

models (panels (b) and (d)). No clear anomalies can be seen, thus none of the fits seems to be accidental. In Figure 11 we plot the contours of  $\chi^2/dof$  and  $\chi^2_F/dof_F$  for the same models in the space of the ratio of temperatures  $T_p/T_e$  at  $6M$  and spin inclination angle  $\theta$ . First, note that good fits for  $\chi^2_F/dof_F$  (panels (a) and (c)) have almost constant electron temperature  $T_e$  correspondent to a range of inclination angles  $\theta$ . A much smaller range in  $\theta$  is allowed according to full  $\chi^2/dof$  (panels (b) and (d)) with similar behavior for RMS-field spin and linear-averaged spin solutions with  $a_* = 0.9$ .

We illustrated in Figure 7 how the best-fitting models with different spins perform. Now we visualize in Figure 12 the differences between  $\chi^2/dof$  and  $\chi^2_F/dof_F$  for the best-fitting models. Solid curves on both panels

represent RMS-field models, whereas dashed curves represent models with linear-averaged magnetic field. Blue curves on both panels show the total reduced  $\chi^2/dof$ , whereas red curves on the left panel correspond to  $\chi^2_F/dof_F$  for flux spectrum fitting. Panel (a) shows the best  $\chi^2_F/dof_F$  and  $\chi^2/dof$  as functions of spin  $a_*$ . We see that the best  $\chi^2_F/dof_F$  for flux fitting is below unity for high spins  $a_* = 0.7, 0.9, 0.98$ , whereas good fits cannot be achieved for low spins  $a_* = 0, 0.5$ . High spins are favored. The same is true when we fit polarized observations.

The RMS-field model with spin  $a_* = 0.9$  exhibits the lowest reduced  $\chi^2$ . However, the value is not close to unity, which indicates significant room is available to improve the model. The linear-averaged model with spin  $a_* = 0.5$  seems to have the lowest reduced  $\chi^2$  over linear-

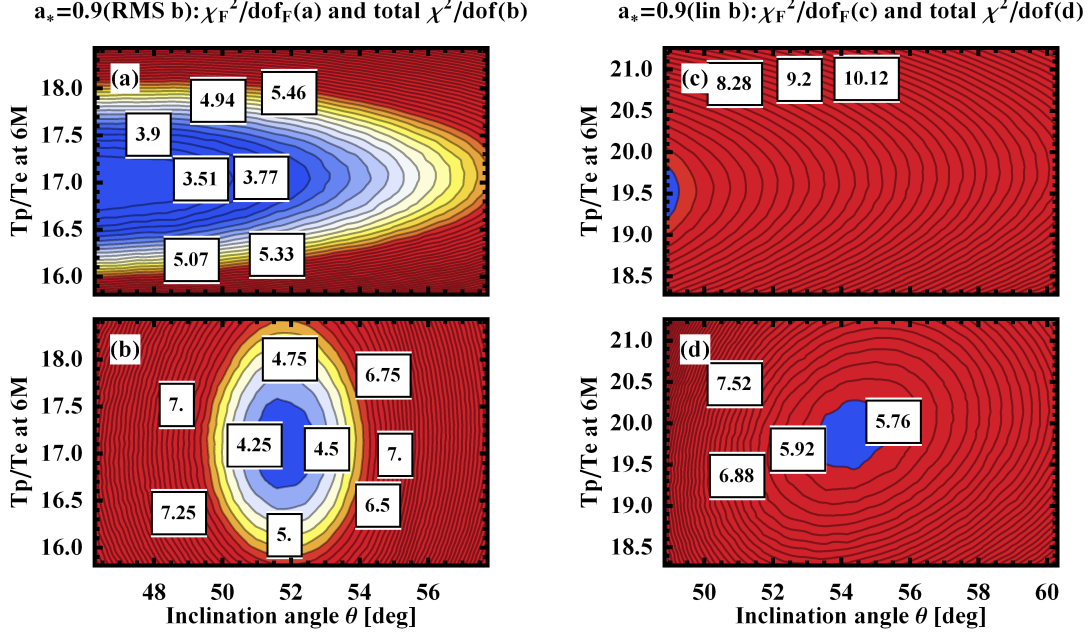


**Figure 11.** Behavior of  $\chi^2$  near the best-fitting models with spin  $a_* = 0.9$ : RMS-field model with RMS magnetic field  $\mathbf{b}$  (left column) and a model with linear averaged  $\mathbf{b}$  (right column) with changing ratio of temperatures  $T_p/T_e$  at  $6M$  and inclination angle of BH spin  $\theta$ . Contours of  $\chi_F^2/\text{dof}_F$  for flux fitting are in the upper row, contours for full  $\chi^2/\text{dof}$  are in the lower row.

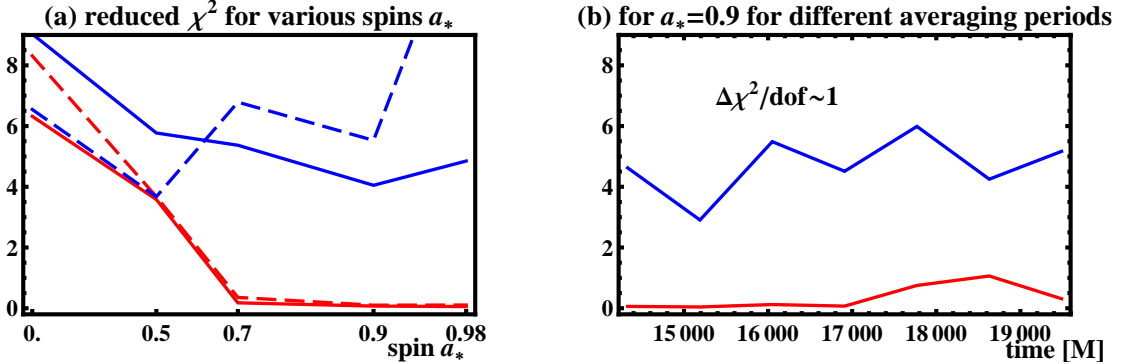


**Figure 12.** The lowest reduced  $\chi^2$  for fits with each spin  $a_*$ . Blue upper curves correspond to total  $\chi^2/\text{dof}$  for fitting total flux at 7 frequencies, LP fraction at 3 frequencies and CP at 2 frequencies. Red lower curves correspond to  $\chi_F^2/\text{dof}_F$  for fitting of total flux at 7 frequencies. Solid curves correspond to RMS-field  $\mathbf{b}$  models, whereas dashed lines show linear-averaged  $\mathbf{b}$  models. Reduced  $\chi^2$  for spins  $a_* = 0, 0.5, 0.7, 0.9, 0.98$  are shown on figure (a) for the models averaged over the period 14000 – 20000M. Spin  $a_* = 0.9$  gives the lowest reduced  $\chi^2$ . Reduced  $\chi^2$  for spin  $a_* = 0.9$  are shown on panel (b) for RMS-field models averaged over smaller intervals within the 14000 – 20000M time-range. No significant secular drift is present for converged simulations, though the variations of  $\chi^2/\text{dof}$  are quite large reaching  $\pm 1$ .

averaged models. However, as discussed previously, we consider models with the RMS-field version of  $\mathbf{b}$  to be more physical compared to models with linear-averaged  $\mathbf{b}$ , thus we stick to RMS-field models in our analysis. We illustrate the stability of the best fit on panel (b) of Figure 12. There we show the best  $\chi^2/\text{dof}$  for RMS-field models with spin  $a_* = 0.9$  for several averaging periods. The periods have the duration 860M within the range 14000 – 20000M: 13900 – 14760M interval, 14760 – 15620M interval etc. The values of  $\chi^2/\text{dof}$  are depicted on panel (b) at the interval middles: 14330M, 15190M etc. The values of  $\chi^2/\text{dof}$  fluctuate between intervals by up to  $\Delta\chi^2/\text{dof} \sim 1$ , which is comparable to

the difference  $\Delta\chi^2/\text{dof} = 1.5$  between spin  $a_* = 0.5$  and spin  $a_* = 0.9$  models. Thus, we can only conclude that the RMS-field model with spin  $a_* = 0.9$  is marginally better than the models with spins  $a_* = 0.5, 0.7, 0.98$ . Changes of best  $\chi^2/\text{dof}$  with time show no secular trend, thus indirectly proving convergence of the simulations (see Section 3.6 for the discussion of convergence).

There is another way to test the dynamical models against observations. The intrinsic image size was recently measured (Doeleman et al. 2008) with the VLBI technique. Total flux  $F = 2.4$  Jy at 230 GHz and correlated flux  $F_{\text{corr}} \approx 0.35$  Jy at 3.5 G $\lambda$  SMT-JCMT baseline were simultaneously measured. We plot this correlated flux with  $3\sigma$  error bar in Figure 13 and compare

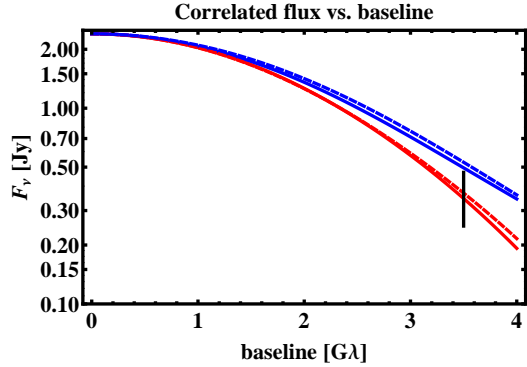


**Figure 13.** Correlated fluxes as functions of baseline normalized to the 2.4 Jy total flux for best-fitting spin  $a_* = 0.9$  model with linear averaged  $\mathbf{b}$  (dashed lines) and the spin  $a_* = 0.9$  RMS-field model with RMS  $\mathbf{b}$  (solid lines). For each model the upper line shows the smallest size (largest correlated flux) over all position angles of BH spin axis, the lower dashed line shows the largest size (smallest correlated flux) over all position angles. An observation from Doeleman et al. (2008) with  $3\sigma$  error bars at baseline 3.5 G $\lambda$  is drawn for comparison. Models fit quite well the observed emission region size.

it to simulated correlated fluxes, normalizing the total flux to 2.4 Jy. To simulate the correlated flux we follow Fish et al. (2009) and employ a Gaussian interstellar scattering ellipse with half-widths at half-maximum  $7.0 \times 3.8 G\lambda$  with position angle  $170^\circ$  east of north. We vary the position angle of BH spin and plot correlated flux curves with the largest (solid line) and the smallest (dashed line) correlated flux at 3.5 G $\lambda$ . The correlated fluxes for spin  $a_* = 0.9$  best-fitting models are shown: blue (dark) lines correspond to maximum correlated fluxes and red (light) lines correspond to minimum correlated fluxes. Solid lines correspond to the RMS-field model and dashed lines to the model with linear-averaged  $\mathbf{b}$ . Both types of models are consistent with observations, but slightly overproduce the correlated flux, which indicates the size of the shadow is slightly underpredicted. We discuss the possible ways to reconcile observations and simulations in the next section.

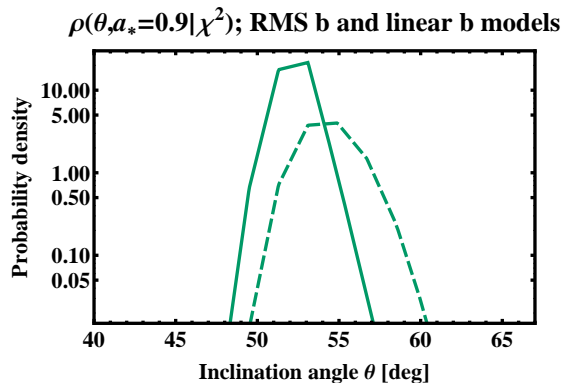


**Figure 14.** Marginalized over heating parameter  $C$  and accretion rate  $\dot{M}$ , the probability densities  $\rho(\theta, a_* = 0.9 | \chi^2)$  over inclination angle  $\theta$  for spin  $a_* = 0.9$ . Shown are peaks for the RMS-field model (solid line) and linear-averaged model (dashed line). The peaks do overlap, which allows for a robust estimate of the inclination angle. The values  $\theta = 50^\circ - 59^\circ$  are allowed.

Having analyzed the best fits and compared the reduced  $\chi^2$ , we can make a conservative estimate of the model parameters. Let us start with the inclination an-

gle of BH spin  $\theta$  ( $\theta = 90^\circ$  for the edge-on disk). On Figure 14 we plot probability density  $\rho(\theta, a_* = 0.9 | \chi^2)$  for inclination angle for two models with spin  $a_* = 0.9$ . This quantity represents probability density of the model given the data (31) integrated over heating constant and accretion rate

$$\rho(\theta, a_* = 0.9 | \chi^2) \propto \iint \rho(a_* = 0.9, \theta, \dot{M}, C | \chi^2) dC d\dot{M}. \quad (33)$$

Both curves are normalized to give  $\int \rho(\theta, a_* = 0.9 | \chi^2) d\theta = 1$ . The solid line corresponds to a RMS-field model, whereas the dashed line to a linear-averaged model. The probable range of  $\theta$  is quite small in each model, which gives tight constraints on  $\theta$  in that particular model. The confidence interval  $\theta(\text{RMS } \mathbf{b})$  for a RMS-field spin  $a_* = 0.9$  model overlaps with the interval for a linear-averaged model  $\theta(\text{lin } \mathbf{b})$ . Thus, a narrow conservative estimate  $\theta_{\text{est}}$  can be provided:

$$\begin{aligned} \theta(\text{RMS } \mathbf{b}) &= 53^\circ \pm 3^\circ, \\ \theta(\text{lin } \mathbf{b}) &= 55^\circ \pm 4^\circ, \\ \theta_{\text{est}} &= 50^\circ - 59^\circ. \end{aligned} \quad (34)$$

The best  $\theta$  for RMS-field models with spins  $a_* = 0.5, 0.7, 0.98$  are, correspondingly,  $\theta = 66^\circ, 62^\circ, 54^\circ$ . Thus, our conservative estimate is quite robust.

Likewise, we can calculate the expectation value and 90% confidence intervals for electron temperature  $T_e$  at  $6M$  for spin  $a_* = 0.9$  models:

$$\begin{aligned} T_e(\text{RMS } \mathbf{b}) &= (4.62 \pm 0.56) \cdot 10^{10} \text{ K}, \\ T_e(\text{lin } \mathbf{b}) &= (2.86 \pm 0.16) \cdot 10^{10} \text{ K}, \\ T_{e,\text{est}} &= (2.7 - 5.2) \cdot 10^{10} \text{ K}. \end{aligned} \quad (35)$$

The accretion rate  $\dot{M}$  has large variations between models:

$$\begin{aligned} \dot{M}(\text{RMS } \mathbf{b}) &= (1.09 \pm 0.13) \times 10^{-8} M_\odot \text{ year}^{-1}, \\ \dot{M}(\text{lin } \mathbf{b}) &= (1.50 \pm 0.15) \times 10^{-8} M_\odot \text{ year}^{-1}, \\ \dot{M}_{\text{est}} &= (0.9 - 1.7) \times 10^{-8} M_\odot \text{ year}^{-1}. \end{aligned} \quad (36)$$

The RMS-field model with spin  $a_* = 0.5$  gives very different accretion rate  $\dot{M}(0.5)_{\text{est}} \approx 4 \times 10^{-8} M_\odot \text{ year}^{-1}$ .

There is one more quantity we can estimate: the position angle (PA) of BH spin. Similarly to Huang et al. (2009a), we rely on observed intrinsic EVPA  $\approx 111.5^\circ$  at 230 GHz and EVPA  $\approx 146.9^\circ$  at 349 GHz (see § 2). For the model to fit the difference in EVPA, we add a Faraday rotation screen far from the BH with constant rotation measure (RM). Then we compute the required RM and the intrinsic PA to fit the simulated EVPAs at 230 and 349 GHz. The best-fitting RMS-field model with  $a_* = 0.9$  gives PA =  $121^\circ$  east of north, whereas the best-fitting linear-averaged model with spin  $a_* = 0.9$  requires PA =  $123^\circ$ . The correspondent 90% confidence intervals are

$$\begin{aligned} \text{PA}(\text{RMS } \mathbf{b}) &= 121^\circ \pm 20^\circ, \\ \text{PA}(\text{lin } \mathbf{b}) &= 123^\circ \pm 20^\circ, \\ \text{PA}(\text{est}) &= 101^\circ - 143^\circ, \end{aligned} \quad (37)$$

where the error is dominated by the observational error of EVPA determination (see Table 1). The estimated



position still has large uncertainty, what precludes us from tightening the size estimates (see Figure 13) from the models. It is reasonable to employ the minimum and maximum correlated fluxes found over all orientations.

With the estimated orientation of the BH spin, we can plot an image of radiation intensity from near the event horizon. Figure 15 shows images of total intensity  $I_\nu$  for the spin  $a_* = 0.9$  best-fitting RMS-field solution on the upper left panel, the spin  $a_* = 0.9$  best-fitting linear-averaged solution on the lower left panel; LP intensity and CP intensity plots for best spin  $a_* = 0.9$  RMS-field model are shown on the upper right and lower right, correspondingly. Blue (predominant) color on CP plot depicts the regions with negative CP intensity and red (subdominant) color depicts the regions with positive CP intensity. The total  $V$  flux from this solution is negative ( $V < 0$ ). The streamlines on LP plot are aligned with EVPA direction at each point. The spin axis is rotated by PA = 121° east of north for spin  $a_* = 0.9$  RMS-field solution and by PA = 123° for the linear-averaged solution. The spin axis is inclined at  $\theta$  to the line of sight, so that the either right (west) or left (east) portions of the flow are closer to the observer. The color schemes on all the plots are nonlinear with correspondent calibration bars plotted on the sides. The numbers at the top of calibration bars denote normalizations.

## 8. DISCUSSION AND CONCLUSIONS

Let us compare our results with estimates of Sgr A\* accretion flow and BH parameters made by other groups. Two separate searches for spin based on GR numerical simulations have been reported so far: Moscibrodzka et al. (2009) and Dexter et al. (2010). The first paper browses the set of spins from  $a_* = 0.5$  to 0.98 for 2D GRMHD simulations, fits X-Ray flux, 230 GHz flux, and slope at this frequency, and finds at least one model for each spin consistent with observations (see Table 3 therein). Their best-bet model has  $a_* = 0.9$ . Dexter et al. (2010) focuses on a set of 3D GRMHD, fits 230 GHz flux and size estimates and provides the table of spin probabilities with  $a_* = 0.9$  again having the highest  $P(a)$ . If we were only to consider spectrum fitting, then our results would perfectly conform to the picture with high spin  $a_* \sim 0.9$  being most likely. When we fit spectrum, LP and CP fractions, spin  $a_* = 0.9$  solutions also give lower reduced  $\chi^2$ . We are unable to provide narrow constraints on  $a$ , and neither do other groups. Other spin estimates have been based on analytic models. Broderick et al. (2009, 2010) favor  $a_* = 0$  solutions, Huang et al. (2009b) favor  $a_* < 0.9$  although they do not explore their full model parameter space. Another poorly constrained quantity is the accretion rate. Our conservative estimate  $\dot{M}_{\text{est}} = (0.9 - 1.7) \cdot 10^{-8} M_\odot \text{year}^{-1}$  is broad. Good models in Moscibrodzka et al. (2009) have similar  $\dot{M}$  of  $\dot{M} = 0.9 \cdot 10^{-8} M_\odot \text{year}^{-1}$ , but  $\dot{M} = 12 \cdot 10^{-8} M_\odot \text{year}^{-1}$  is also found among good fits. Dexter et al. (2010) found relatively tight boundaries for 90% confidence interval of  $\dot{M}$  by looking at spin  $a_* = 0.9$  solutions by incorporating flow size in  $\chi^2$  analysis. Our estimate is consistent with, but slightly narrower than the full range  $\dot{M} = 5_{-2}^{+15} \times 10^{-9} M_\odot \text{year}^{-1}$  (90%) in Dexter et al. (2010). Note, that Dexter et al. (2009) got much lower

accretion rate  $\dot{M}(0.9) = (1.0 - 2.3) \times 10^{-9} M_\odot \text{year}^{-1}$  as they assumed the equality of proton and electron temperatures  $T_e = T_p$ .

In addition to spin and accretion rate we can constrain inclination angle  $\theta$  and electron temperature  $T_e$  at  $6M$ . Our conservative estimate is  $\theta_{\text{est}} = 50^\circ - 59^\circ$ , which is the narrowest of all estimates in the literature. This  $\theta$  is fully consistent with the estimates  $\theta = 50^\circ$  in Broderick et al. (2009); Dexter et al. (2010). Huang et al. (2009a) and Huang et al. (2009b) favor slightly lower  $\theta = 40^\circ, 45^\circ$ , but have large error bars. Inclusion of polarized observations also puts stricter limits on  $T_e$ . Moscibrodzka et al. (2009) and Dexter et al. (2010) set constant  $T_p/T_e$ , whereas Huang et al. (2009a) and us calculate the profile of  $T_e$ . In all models,  $T_e$  is a shallow function of radius, which made Dexter et al. (2010) estimate the “common”  $T_e = (5.4 \pm 3.0) \times 10^{10}$  K, which is the quantity calculated supposedly still at certain distance from the BH center. Setting this distance to  $6M$  we arrive at the consistent, but narrower conservative estimate  $T_{e,\text{est}} = (2.7 - 5.2) \times 10^{10}$  K. There are two kinds of constraints on BH spin position angle: 230 GHz correlated flux fitting and EVPA fitting. The first path was adopted in Broderick et al. (2009) and Dexter et al. (2010) with the results PA =  $(-20^\circ) - (-70^\circ) = (110^\circ) - (180^\circ)$ . These PAs agree quite well with polarization data. Meyer et al. (2007) predicts the range PA =  $60^\circ - 108^\circ$ , whereas Huang gets either PA  $\approx 115^\circ$  (Huang et al. 2009b) or PA  $\approx 140^\circ$  (Huang et al. 2009a) depending on the model without calculating the range. Our estimate of PA =  $101^\circ - 143^\circ$  is quite narrow, and agrees well with Meyer et al. (2007) and other groups. Significantly larger error bars, and the fact that very few size observations are available, make PA estimates from size less reliable than those from EVPA. In addition, the size of the flow may depend substantially on luminosity state (Broderick et al. 2009) or the presence of non-thermal structures, spiral waves, and other features.

In some astrophysical sources PA is directly known from spatially resolved jets, and Sgr A\* may be one such source. A tentative jet feature was revealed in X-rays by Muno et al. (2008), Fig. 8 with  $\text{PA}_{\text{jet}} = 120^\circ$ . The mean of our conservative PA interval practically coincides with  $\text{PA}_{\text{jet}}$ , which provides support for a jet hypothesis for this feature.

Besides the estimates of accretion rate and flow properties based on the inner flow, there exist estimates based on the outer flow. Shcherbakov & Baganoff (2010) constructed an inflow-outflow model with conduction and stellar winds, which provided an excellent agreement to X-ray surface brightness profile observed by *Chandra*. Their model had an accretion rate  $\dot{M} = 6 \cdot 10^{-8} M_\odot \text{year}^{-1}$  and electron temperature  $T_e = 3.6 \times 10^{10}$  K at  $6M$  (Note that gravitational radius is defined as  $r_g = 2M$  in Shcherbakov & Baganoff (2010)). from the center showing a great agreement with present results. Thus, the radial extensions of density to large radius is justified. We constrain density in the outer flow by X-ray observations (Shcherbakov & Baganoff 2010) and in the inner flow by sub-mm observations. The resultant density profile

$$\rho \propto r^{-\beta}, \quad \beta = 0.80 - 0.90 \quad (38)$$

is a quite robust estimate. Density power-law index

images of total and polarized intensities for best-fitting models

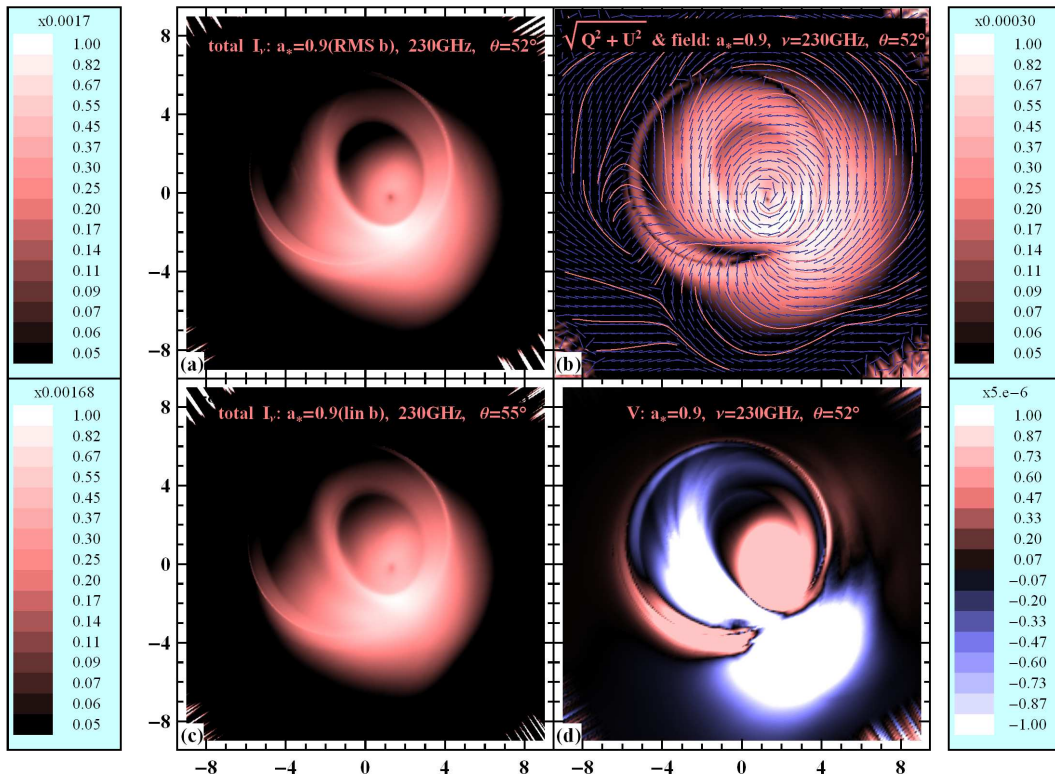


**Figure 15.** Images of polarized intensities for the best-fitting models: total intensity for spin  $a_* = 0.9$  linear-averaged model (lower left); intensities for  $a_* = 0.9$  RMS-field model: total intensity (upper left), linear polarized intensity and streamlines along EVPA (upper right), and circular polarized intensity (lower right). Distances are in the units of BH mass  $M$ . Images are rotated in the picture plane to fit the best spin PA: PA =  $121^\circ$  for the RMS-field model and PA =  $123^\circ$  for the linear-averaged model. Individual calibration bars are on the sides of correspondent plots. The ill-defined polar region does not contribute significantly to the emission.

$\beta$  lies between  $\beta = 1.5$  for ADAF flow (Narayan & Yi 1995) and  $\beta = 0.5$  for the convection-dominated accretion flow (Narayan, Igumenshchev, & Abramowicz 2000; Quataert & Gruzinov 2000). However, the modification of the power-law index from the steep ADAF profile is likely due to conduction for Sgr A\*, not convection.

In the present paper we combined several sophisticated techniques to arrive at our conclusions. Let us now examine the viability of the approaches employed. The dynamical model, despite being based on 3D GRMHD simulations, incorporates averaging and strong approximations. Despite simulating many Keplerian orbits in the region within  $25M$ , the slopes of density  $n_e$  and temperatures  $T_p$  and  $T_e$ , fixed at the outer flow, break at a radius of roughly  $25M$ . This suggests one needs to simulate an even larger domain in radius and potentially add other physical effects such as conduction (Johnson & Quataert 2007; Sharma et al. 2008; Shcherbakov & Baganoff 2010). Simulations with larger dynamic range will also help to constrain the Faraday rotation, which happens for the present models partially outside of the simulated domain. The proper simulation of the polar region of the flow may be important as well. At present we artificially limit the magnetization and temperature there. If we do not, then the numerical artifacts associated with excessive numerical dissipation and heating appear, similar to those in Moscibrodzka et al. (2009). The unanimous decision in favor of  $a_* = 0.9$  spin

for similar types of fitting over the simulation-based models gives a hope that the simulations of different groups are sufficiently similar and any simulation and averaging of the sort is representative.

If the non-thermal electrons provide most of energy for sub-mm peak, then this may potentially invalidate the spin estimates (Shcherbakov & Huang 2011).

Radiative transfer, in turn, has its own assumptions. Our emissivities in the special synchrotron approximation are good enough, providing e.g. 2% agreement with exact emissivities (Leung, Gammie & Noble 2009; Shcherbakov & Huang 2011) for  $b = 20$  G,  $\theta_B = 1$  rad,  $T_e = 6.9 \cdot 10^9$  K, and observed frequency  $\nu = 100$  GHz. Agreement is better for larger  $T_e$ . The non-polarized radiative transfer of total intensity (Moscibrodzka et al. 2009; Dexter et al. 2010) has an intrinsic error in comparison with polarized radiative transfer with the same total emissivity  $\varepsilon_I$ , however the error is only 1–5%. We use the averaged dynamical model to calculate radiation and do not perform the statistical analysis of radiation from many simulation shots. This is a strong approximation, which cannot be easily justified and requires future improvement. Polarized radiative transfer appears to be much slower than unpolarized, and the present computation took 17k CPU-hours on a supercomputer to explore the full parameter space. Reliable statistics of radiation over many snapshots may require up to 1M CPU-hours, and is not viable at present.

There are still unaccounted sources of error. The mass of the BH in the Galactic Center is known to within 10% (Ghez et al. 2008) and the distance is known to 5%. We do not perform a detailed analysis here, but it seems that these uncertainties would not lead to significant changes in our predictions. A simple shift to slightly lower spin should be able to mimic the effect of smaller BH or a BH at larger distance from us.

Apart from questions of modeling, the improvement of observational data can lead to further insights on the flow structure and more reliable estimates of BH spin. The detailed comparison of flux, LP, and CP curves in Figure 7 show that the models with spin  $a_* = 0.5$  and spin  $a_* = 0.9$  have discrepancies in these regions not constrained by observations. In particular, the CP fractions at 145 GHz are different. EVPA data needs improvement as well. Despite some statistics available at 230 GHz and 349 GHz, the variability of EVPA is about  $20^\circ$ , which translates to  $\pm 20^\circ$  ( $3\sigma$ ) uncertainty of the mean PA, whereas the modeling uncertainty is only several degrees. More observations of EVPA at these frequencies will help to find the Faraday rotation measure more precisely and constraint the PA of BH spin. An alternative is to observe at higher frequencies  $\nu \geq 690$  GHz, where both the Faraday rotation effect and fluctuations of the intrinsic emission EVPA are small. Another important quantity is LP at 88 GHz, whose observations are only reported in 2 papers. Variations in simulated LP(88GHz) are quite large between the best models (see Figure 7). Refinement of the observed mean  $\log(\text{LP}(88\text{GHz}))$  could potentially help discriminate better between the  $a_* = 0.5$  and  $a_* = 0.9$  spin solutions. A measurement of the emitting region size or the correlated flux is also promising. Despite the correlated flux at 230 GHz being measured at the SMT-JCMT  $3.5G\lambda$  baseline, the statistics of this measurement are needed to capture variations of  $F_{\text{corr}}$  over at least a year to be comparable with the statistics of total flux. The correlated flux observations are currently being accumulated (Fish et al. 2011). The correlated flux at this baseline is exponentially sensitive to the physical flow size, which can make slightly brighter states have significantly lower  $F_{\text{corr}}$ . As a caveat, the conclusion on image sizes may depend on the behavior of matter in the ill-defined polar regions. Our models do not exhibit significant emission from high latitudes at 230 GHz (see Figure 15) or anywhere above 88 GHz.

The present work offers an improvement over the previous estimates of the Sgr A\* spin, inclination, and accretion flow properties, though there is still significant room for improvement. Future work would incorporate more statistics from recent polarized observations in the sub-mm. Future 3D GRMHD simulations would have higher dynamic range converging at  $r > 50M$  and likely have a more pronounced outflow. Adding Comptonization to radiative transfer would one to test the quiescent X-rays luminosity  $L \approx 4 \cdot 10^{32} \text{erg s}^{-1}$  within 2 – 10 keV (Shcherbakov & Baganoff 2010). So far we have focused on the mean state and discarded the information of simultaneity. These data will be used in future analysis of observations to tighten the error bars. The time variability properties can be found from the simulations and compared to the observed ones. In particular, “jet lags” (Yusef-Zadeh et al. 2008; Maitra, Markoff & Falcke 2009) and quasi-periodic oscil-

lations (QPOs) (Genzel et al. 2003; Eckart et al. 2006; Miyoshi 2010) should be investigated using the simulations.

## 9. ACKNOWLEDGEMENTS

The authors are grateful to Lei Huang for checking various emissivity prescriptions, to Ramesh Narayan for extensive discussions and comments, to Avi Loeb, Avery Broderick, James Moran, Alexander Tchekhovskoy, Cole Miller, Steven Cranmer for insightful comments. The numerical simulations and the radiative transfer calculations in this paper were partially run on the Odyssey cluster supported by the FAS Sciences Division Research Computing Group and were partially supported by NSF through TeraGrid resources provided by NCSA (Abe), LONI (QueenBee), and NICS (Kraken) under grant numbers TG-AST080025N and TG-AST080026N. The paper is partially supported by NASA grants NNX08AX04H (RVS&Ramesh Narayan), NNX08AH32G (Ramesh Narayan), NSF Graduate Research Fellowship (RFP), and NASA Chandra Fellowship PF7-80048 (JCM).

## REFERENCES

- Aitken, D. K., Greaves, J., Chrysostomou, A., Jenness, T., Holland, W., Hough, J. H., Pierce-Price, D., Richer, J. 2000, *ApJ*, 534, 173
- An, T., Goss, W. M., Zhao, J.-H., Hong, X. Y., Roy, S., Rao, A. P., Shen, Z.-Q. 2005, *ApJ*, 634, 49
- Baganoff, F. K., et al. 2001, *Nature*, 413, 45
- Baganoff, F. K., et al. 2003, *ApJ*, 591, 891
- Balbus, S. A., & Hawley, J. F. 1998, *Reviews of Modern Physics*, 70, 1
- Beckwith K., Hawley J. F., Krolik J. H., 2008a, *ApJ*, 678,1180
- Berger, J. O. 1985, “Statistical Decision Theory and Bayesian Analysis”, (New York: Springer-Verlag)
- Blandford, R. D., & Begelman, M. C. 1999, *MNRAS*, 303L, 1
- Bower, G. C., Falcke, H., Backer, D. C. 1999a, *ApJ*, 523, L29
- Bower, G. C., Wright, M. C. H., Backer, D. C., Falcke, H. 1999b, *ApJ*, 527, 851
- Bower, G. C., Wright, M. C. H., Falcke, H., Backer, D. C. 2001, *ApJ*, 555, 103
- Bower, G. C., Falcke, H., Sault, R. J., Backer, D. C. 2002, *ApJ*, 571, 843
- Bower, G. C., Wright, M. C. H., Falcke, H., Backer, D. C. 2003, *ApJ*, 588, 331
- Bower, G. C., Falcke, H., Wright, M. C., Backer, & Donald C. 2005, *ApJ*, 618, 29
- Broderick, A. E., Fish, V. L., Doeleman, S. S., Loeb, A 2009, *ApJ*, 697, 45
- Broderick, A. E., Fish, V. L., Doeleman, S. S., Loeb, A 2010, *astro-ph/1011.2770*
- Chakrabarti S. K., 1985a, *ApJ*, 288, 1
- Chakrabarti S. K., 1985b, *ApJ*, 294, 383
- Chan, C.-K., Liu, S., Fryer, C. L., Psaltis, D., O’zel, F., Rockefeller, G., Melia, Fulvio 2009, *ApJ*, 701, 521
- De Villiers J.-P., Hawley J. F., Krolik J. H., 2003, *ApJ*, 599, 1238
- Dexter, J., Agol, E., Fragile, P. C. 2009, *ApJ*, 703, 142
- Dexter, J., Agol, E., Fragile, P. C., McKinney, J. C. 2010, *ApJ*, 717, 1092
- Dolence, J. C., Gammie, C. F., Moscibrodzka, M., Leung, P. K. 2009, *ApJS*, 184, 387
- Doeleman S. S. et al 2001, *AJ*, 121, 2610
- Doeleman, S. S. et al. 2008, *Nature*, 455, 78
- Eckart, A., Schödel, R., Meyer, L., Trippe, S., Ott, T., Genzel, R. 2006, *A&A*, 455, 1
- Falcke, H., Goss, W. M., Matsuo, H., Teuben, P., Zhao, J.-H., Zylka, R. 1998, *ApJ*, 499, 731
- Fish, V. L., Broderick, A. E., Doeleman, S. S., Loeb, A. 2009, *ApJ*, 692, L14
- Fish, V. L., et al. 2011, *ApJ*, 727, 36

- Fragile, P. C., Lindner, C. C., Anninos, P., & Salmonson, J. D. 2009, *ApJ*, 691, 482
- Fuerst, S. V., Wu, K. 2004, *A&A*, 424, 733
- Gammie, C. F., McKinney, J. C., Toth, G. 2003, *ApJ*, 589, 444
- Gammie, C. F., Shapiro, S. L., McKinney, J. C. 2004, *ApJ*, 602, 312
- Gammie, C. F., Leung, P. K. 2010, *MNRAS*, submitted
- Ghez, A. M., et al. 2008, *ApJ*, 689, 1044
- Ghosh, S., & Mukhopadhyay, B. 2007, *ApJ*, 667, 367
- Genzel, R., Schödel, R., Ott, T., Eckart, A., Alexander, T., Lacombe, F., Rouan, D., Aschenbach B. 2003, *Nature*, 425, 934
- Goldston, J. E., Quataert, E., Igumenshchev, I. V. 2005, *ApJ*, 621, 785
- Hamaker J. P., Bregman J. D., 1996, *A & AS*, 117, 161
- Herrnstein, R. M., Zhao, J.-H., Bower, G. C., Goss, W. M. 2004, *AJ*, 127, 3399
- Homan, D. C., Lister, M. L., Aller, H. D., Aller, M. F., Wardle, J. F. C. 2009, *ApJ*, 696, 328
- Huang, L., Liu, S., Shen, Z.-Q., Cai, M. J., Li, H., & Fryer, C. L. 2008, *ApJ*, 676L, 119
- Huang, L., Liu, S., Shen, Z.-Q., Yuan, Y.-F., Cai, M. J., Li, H., & Fryer, C. L. 2009a, *ApJ*, 703, 557
- Huang, L., Takahashi, R., Shen, Z.-Q. 2009b, *ApJ*, 706, 960
- Igumenshchev, I. V. 2008, *ApJ*, 677, 317
- Jaynes, E. T., Bretthorst, G. L. 2003, "Probability Theory", (Cambridge: Cambridge University Press)
- Johnson, B. M., Quataert, E. 2007, *ApJ*, 660, 1273
- Komissarov S. S., McKinney J. C., 2007, *MNRAS*, 377, L49
- Krichbaum T. P. 1998, *A&A*, 335, L106
- Krichbaum, T. P., Graham, D. A., Bremer, M., Alef, W., Witzel, A., Zensus, J. A., Eckart, A. 2006, *JPhCS*, 54, 328
- Legg, M. P. C., Westfold, K. C., 1968, *ApJ*, 154, 499
- Leung, P. K., Gammie, C. F., Noble S. C. 2009, *ApJ*, submitted
- Li, J., Shen, Z.-Q., Miyazaki, A., Huang, L., Sault, R. J., Miyoshi, M., Tsuboi, M., Tsutsumi, T. 2008, *JPhCS*, 131, 2007
- Lo, K. Y., Shen, Z.-Q., Zhao, J.-H., Ho, P. T. P. 1998, *ApJ*, 508, L61
- Lu, R.-S., Krichbaum, T. P., Eckart, A., König, S., Kunneriath, D., Witzel, G., Witzel, A., Zensus, J. A. 2008, *JPhCS*, 131, 2059
- Macquart, J.-P., Bower, G. C., Wright, M. C. H., Backer, Donald C., Falcke, H. 2006, *ApJ*, 646, L111
- Mahadevan, R. 1998, *Nature*, 394, 651
- Maitra, D., Markoff, S., Falcke, H. 2009, *A&A*, 508, 13
- Marrone, D. P., Moran, J. M., Zhao, J.-H., Rao, R. 2006a, *JPhCS*, 54, 354
- Marrone, D. P., Moran, J. M., Zhao, J.-H., Rao, R. 2006b, *ApJ*, 640, 308
- Marrone, D. P., Moran, J. M., Zhao, J., & Rao R., 2007, *ApJ*, 654L, 57
- Marrone D. P., et al. 2008, *ApJ*, 682, 373
- Mauerhan, J. C., Morris, M., Walter, F., Baganoff, F. K. 2005, *ApJ*, 623, 25
- McKinney, J. C., & Gammie, C. F. 2004, *ApJ*, 611, 977
- McKinney, J. C. 2006, *MNRAS*, 367, 1797
- McKinney, J. C. 2006, *MNRAS*, 368, 1561
- McKinney, J. C., & Blandford, R. D. 2009, *MNRAS*, 394, L126
- McKinney J. C., Narayan R., 2007a, *MNRAS*, 375, 513
- McKinney J. C., Narayan R., 2007b, *MNRAS*, 375, 531
- Melrose, D. B. 1971, *Ap&SS*, 12, 172
- Meyer, L., Schödel, R., Eckart, A., Duschl, W. J., Karas, V., Dovčiak, M. 2007, *A&A*, 473, 707
- Mignone, A., McKinney, J. C. 2007, *MNRAS*, 378, 1118
- Miyazaki, A., Tsutsumi, T., Tsuboi, M. 2004, *ApJ*, 611, 97
- Miyoshi, M., Shen, Z.-Q., Oyama, T., Takahashi, R., Kato, Y. 2010, *astro-ph/0906.5511*
- Moscibrodzka, M., Gammie, C. F., Dolence, J. C., Shiokawa, H., Leung, P. K. 2009 *ApJ*, 706, 497
- Muno, M. P., et al. 2008, *ApJ*, 673, 251
- Munoz, D., Marrone, D., Moran, J. 2009, *Bulletin of the AAS*, 41, 761
- Narayan, R., & Yi, I. 1995, *ApJ*, 452, 710
- Narayan, R., Yi, I., Mahadevan, R. 1995, *Nature*, 374, 623
- Narayan, R., Mahadevan, R., Grindlay, J. E., Popham, R. G., Gammie, C. 1998, *ApJ*, 492, 554
- Narayan, R., Igumenshchev, I. V., & Abramowicz, M. A. 2000, *ApJ*, 539, 798
- Noble, S. C., Gammie, C. F., McKinney, J. C., Del Zanna, L. 2006, *ApJ*, 641, 626
- Noble, S. C., Krolik, J. H. 2009, *ApJ*, 703, 964
- Özel, F., Psaltis, D., Narayan, R. 2000, *ApJ*, 541, 234
- Pacholczyk, A. G. 1970, "Radio astrophysics. Nonthermal processes in galactic and extragalactic sources", (Freeman: San Francisco)
- Penna, R. F., McKinney, J. C., Narayan, R., Tchekhovskoy, A., Shafee, R., McClintock, J. E. 2010, *MNRAS*, 408, 752
- Quataert, E., & Gruzinov, A. 2000, *ApJ*, 539, 809d
- Rybicki, G. B., & Lightman, A. P. 1979, "Radiative processes in astrophysics." (Wiley-Interscience: New York)
- Sazonov, V. N. 1969, *Soviet Astronomy*, 13, 396
- Serabyn, E., Carlstrom, J., Lay, O., Lis, D. C., Hunter, T. R., Lacy, J. H. 1997, *ApJ*, 490, L77
- Shafee R., McKinney J. C., Narayan R., Tchekhovskoy A., Gammie C. F., McClintock J. E., 2008, *ApJ*, 687, L25
- Sharma, P., Quataert, E., Hammett, G. W., & Stone, J. M. 2007, *ApJ*, 667, 714
- Sharma, P., Quataert, E., Stone, J. M. 2008, *MNRAS*, 389, 1815
- Shcherbakov, R. V. 2008, *ApJ*, 688, 695
- Shcherbakov, R. V., Baganoff F. K. 2010, *ApJ*, 716, 504
- Shcherbakov, R. V., Huang, L. 2010, *MNRAS*, 410, 1052
- Shen, Z.-Q., Lo, K. Y., Liang, M.-C., Ho, P. T. P., Zhao, J.-H. 2005, *Nature*, 438, 62
- Shkarofsky, I. P., Johnston, T. W., Bachynski, M. P. 1966, "The particle kinetics of plasma," (Addison-Wesley Publishing Company: London)
- Tchekhovskoy, A., McKinney, J. C., Narayan, R. 2007, *MNRAS*, 379, 469
- Yuan, F., Markoff, S., & Falcke, H. 2002, *A&A*, 383, 854
- Yuan, F., Quataert, E., Narayan, R. 2004, *ApJ*, 606, 894
- Yusef-Zadeh, F., Wardle, M., Cotton, W. D., Heinke, C. O., Roberts, D. A. 2007, *ApJ*, 668, 47
- Yusef-Zadeh, F., Wardle, M., Heinke, C., Dowell, C. D., Roberts, D., Baganoff, F. K., Cotton, W. 2008, *ApJ*, 682, 361
- Yusef-Zadeh, F., et al. 2009, *ApJ*, 706, 348
- Zhao, J.-H., Young, K. H., Herrnstein, R. M., Ho, P. T. P., Tsutsumi, T., Lo, K. Y., Goss, W. M., Bower, G. C. 2003, *ApJ*, 586, 29

## APPENDIX

## RADIATIVE TRANSFER CONVERGENCE

We have written a novel code for general relativistic polarized radiative transfer. As with any new code, we need to conduct a set of convergence tests to ensure it is working accurately. First, we need to devise metrics for assessing accuracy. In the present paper we model fluxes at 7 frequencies between 88 GHz and 857 GHz, LP fractions at 3 frequencies and CP fractions at 2 frequencies and define  $\chi^2$  as to characterize goodness of fit. We employ a similar quantity  $\chi_H^2/\text{dof}$  to characterize the accuracy of transfer. We define

$$\chi_H^2/\text{dof} = \frac{1}{9} \sum_{i=1}^{12} \frac{(Q_{i,1} - Q_{i,2})^2}{\sigma(Q)^2}, \quad (\text{A1})$$

where  $Q_{i,1}$  are simulated fluxes for one set of auxiliary radiative transfer parameters and  $Q_{i,2}$  are for another set. The errors  $\sigma(Q)$  are the observed errors of the mean, and index  $i$  runs through all fluxes, log LP, and CP

**Table 2**  
Values of  $\chi_H^2/\text{dof}$  for radiative transfer tests over best models.

Test	spin $a_* = 0$	spin $a_* = 0.5$	spin $a_* = 0.7$	spin $a_* = 0.9$	spin $a_* = 0.98$	spin $a_* = 0.9$ (lin $\mathbf{b}$ )
$P_N : 75 \rightarrow 111$	0.012	0.0034	0.0097	0.014	0.0046	0.0070
$P_N : 111 \rightarrow 161$	0.0018	0.0043	0.0017	0.00087	0.0013	0.0012
$P_{ss} : 1.003r_H \rightarrow 1.01r_H$	0.00072	0.0017	0.0018	0.00065	0.00041	0.0010
$P_{ss} : 1.01r_H \rightarrow 1.03r_H$	0.018	0.020	0.018	0.017	0.0073	0.020
$P_{\text{fact}} : 0.8 \rightarrow 1.0$	0.027	0.60	0.073	0.050	0.042	0.11
$P_{\text{fact}} : 1.0 \rightarrow 1.2$	0.013	0.185	0.081	0.039	0.017	0.087
$P_{\text{rhopo}} : Q \rightarrow Q+ = 0.2$	0.027	0.064	0.044	0.097	0.018	0.079
$P_{\text{Upo}} : Q \rightarrow Q- = 0.1$	0.096	0.074	0.021	0.017	0.0063	0.0099
$P_{\text{Bpo}} : -1.5 \rightarrow -1.75$	0.19	0.12	0.0026	0.012	0.0049	0.028

fractions. When one of the models fits the data exactly, then  $\chi_H^2/\text{dof}$  coincides with  $\chi^2/\text{dof}$ . Auxiliary radiative transfer parameters designated by  $P_{\dots}$  include:

1. dimensionless scale  $P_{\text{fact}}$  of the size of integration region in the picture plane,
2. distance from the center  $P_{\text{ss}}$  measured in horizon radii  $r_H$ , where radiative transfer starts,
3. number of points  $P_{\text{snxy}} = N$  along each dimension in picture plane,
4. extension power-law slope of density profile  $P_{\text{rhopo}}$ ,
5. extension slope of internal energy density profile  $P_{\text{Upo}}$ ,
6. extension slope of magnetic field profile  $P_{\text{Bpo}}$ .

Since fluctuations and differences in  $\chi^2/\text{dof}$  between different models reach 1, then values  $\chi_H^2/\text{dof} \lesssim 0.1$  are acceptable, but we in general strive for  $\chi_H^2/\text{dof} < 0.02$ . We set constant  $P_{\text{fact}}$ ,  $P_{\text{ss}}$ ,  $P_{\text{snxy}}$  for all radiative transfer computations, but we cannot check the code accuracy for all models. We check the convergence a posteriori for the best RMS-field models at each spin value. We find reasonable values of parameters  $P_{\dots}$  by trial-and-error method for some well-fitting model and then fix them. The resultant set of auxiliary parameters is  $P_{\text{fact}} = 1$ ,  $P_{\text{ss}} = 1.01r_H$ , and  $P_{\text{snxy}} = 111$ . Whereas the values of  $P_{\text{rhopo}}$  and  $P_{\text{Upo}}$  are fixed by extensions to large radii and density in the inner flow. The tests and the values of  $\chi_H^2$  are in Table 2. The first column describes the test: which quantity we change and how. For example,  $P_{\text{fact}} : 1 \rightarrow 0.8$  means that we tested the convergence of integration region relative size, the value of  $P_{\text{fact}}$  changed from 1 to 0.8. We change only one parameter at a time. Since the power-law slopes  $P_{\text{rhopo}}$  and  $P_{\text{Upo}}$  can vary from model to model, we change them such that rhopo is increased by 0.2 and Upo is decreased by 0.1. This represents variation of density by a factor of 7 and variation of temperature by a factor of 2.5 at the distance  $r_{\text{out}} = 3 \cdot 10^5 M$ , where extension starts from, yet leading to minor changes in  $\chi_H^2/\text{dof} < 0.1$  (see Table 2). Density and temperature at  $r_{\text{out}} = 3 \cdot 10^5 M$  are known better than to within a factor of several (Baganoff et al. 2003; Shcherbakov & Baganoff 2010). Thus, the concerns are invalidated that unjustified power-law extensions of density and temperature to large radii may change substantially the polarized spectrum. We also estimate the influence of magnetic field extension power-law by steepening it from  $(r/M)^{-1.5}$  to  $(r/M)^{-1.75}$ . The resultant  $\chi_H^2/\text{dof} \lesssim 0.2$  are small for such a change, but may be much larger for shallower slopes. The extensions as shallow as  $|\mathbf{b}| \propto (r/M)^{-1}$  may provide better fits to Faraday rotation measure and should be carefully explored. Various extensions of the fluid velocity lead to practically the same polarized intensities.